Planetary period magnetic field oscillations in Saturn's magnetosphere: Postequinox abrupt nonmonotonic transitions to northern system dominance

G. Provan,[1] S. W. H. Cowley,[1] J. Sandhu,[1] D. J. Andrews,[2] and M. K. Dougherty[3]

[1]   We examine the "planetary period" magnetic field oscillations observed in the "core" region of Saturn's magnetosphere (dipole $L \leq 12$), on 56 near-equatorial Cassini periapsis passes that took place between vernal equinox in August 2009 and November 2012. Previous studies have shown that these consist of the sum of two oscillations related to the northern and southern polar regions having differing amplitudes and periods that had reached near-equal amplitudes and near-converged periods ~10.68 h in the interval to ~1 year after equinox. The present analysis shows that an interval of strongly differing behavior then began ~1.5 years after equinox, in which abrupt changes in properties took place at ~6- to 8-month intervals, with three clear transitions occurring in February 2011, August 2011, and April 2012, respectively. These are characterized by large simultaneous changes in the amplitudes of the two systems, together with small changes in period about otherwise near-constant values of ~10.63 h for the northern system and ~10.69 h for the southern (thus, not reversed postequinox) and on occasion jumps in phase. The first transition produced a resumption of strong southern system dominance unexpected under northern spring conditions, while the second introduced comparably strong northern system dominance for the first time in these data. The third resulted in suppression of all core oscillations followed by re-emergence of both systems on a time scale of ~85 days, with the northern system remaining dominant but not as strongly as before. This behavior poses interesting questions for presently proposed theoretical scenarios.

Citation: Provan, G., S. W. H. Cowley, J. Sandhu, D. J. Andrews, and M. K. Dougherty (2013), Planetary period magnetic field oscillations in Saturn's magnetosphere: Postequinox abrupt nonmonotonic transitions to northern system dominance, *J. Geophys. Res. Space Physics*, *118*, 3243–3264, doi:10.1002/jgra.50186.

1.   Introduction

[2]   Despite the near-perfect axisymmetry of Saturn's internal planetary magnetic field [e.g., *Burton et al.*, 2010], observations from Pioneer-11, Voyager-1 and -2, and Cassini have shown that rotating modulations near the ~11 h planetary period are ubiquitous in Saturn's magnetosphere. Such modulations are near-continuously observed in the magnetic field, plasma parameters, energetic particle fluxes, and associated neutral atom emissions, as well as auroral ultraviolet and radio emissions [e.g., *Warwick et al.*, 1981, 1982; *Gurnett et al.*, 1981, 2007, 2010a; *Sandel and Broadfoot*, 1981; *Sandel et al.*, 1982; *Carbary and Krimigis*, 1982; *Espinosa and Dougherty*, 2000; *Krupp et al.*, 2005; *Cowley et al.*, 2006; *Kurth et al.*, 2007; *Southwood and Kivelson*, 2007; *Carbary et al.*, 2007, 2008a, 2008b; *Andrews et al.*, 2008; *Nichols et al.*, 2008, 2010a, 2010b; *Burch et al.*, 2009; *Provan et al.*, 2009a, 2009b; *Clarke et al.*, 2006, 2010a, 2010b; *Wang et al.*, 2010; *Ye et al.*, 2010; *Lamy*, 2011]. Physical discussion has variously invoked spontaneous symmetry breaking in centrifugally driven outflow [*Goldreich and Farmer*, 2007], longitudinal asymmetry in the ring current plasma [*Khurana et al.*, 2009; *Brandt et al.*, 2010], and perturbations driven by rotating wind systems in the polar thermosphere [*Smith*, 2010; *Jia et al.*, 2012], possibly influenced by major atmospheric storms [*Fischer et al.*, 2012]. However, no consensus has yet emerged.

[3]   Analyses of Saturn kilometric radiation (SKR) and auroral hiss emissions, believed to be associated with regions of upward and downward auroral field-aligned currents, respectively, have shown that the modulation periods in the northern and southern hemispheres are distinct, ~10.6 h in the north and ~10.8 h in the south during the postsolstice Saturn southern summer conditions observed during the initial Cassini mission interval from mid-2004 to 2008 [*Kurth et al.*, 2008; *Gurnett et al.*, 2009a, 2009b]. It has also been found, however, that these periods are not fixed [*Galopeau and Lecacheux*, 2000] but vary with Saturn's seasons, converging slowly to a common period of ~10.7 h

[1]Department of Physics and Astronomy, University of Leicester, Leicester, UK.
[2]Swedish Institute of Space Physics, Uppsala, Sweden.
[3]Blackett Laboratory, Imperial College, London, UK.

Corresponding author: G. Provan, Department of Physics and Astronomy, University of Leicester, Leicester LE1 7RH, UK. (gp3@ion.le.ac.uk)

and perhaps crossing over a ~2 year interval centered near to vernal equinox in August 2009 [*Gurnett et al.*, 2010b, 2011; *Lamy*, 2011].

[4] Related results have also been derived from analyses of magnetic field oscillations in Saturn's magnetosphere believed to be produced by the same rotating current systems, these being the principal focus of the present paper. Field oscillations observed at polar latitudes and in the tail lobes have been shown to posses the same distinct varying periods as the corresponding SKR emissions [*Andrews et al.*, 2010b; *Southwood*, 2011; *Provan et al.*, 2012], with no admixture of oscillations from the opposite hemisphere within a ~10% amplitude ratio limit [*Andrews et al.*, 2012]. However, the modulations within the near-equatorial magnetosphere and tail plasma sheet consist of the superposition of both northern- and southern-period oscillations, giving rise to phase and amplitude variations in the combined disturbance as the two oscillations interfere over their beat cycle [*Provan et al.*, 2011, 2012; *Andrews et al.*, 2012]. Southern-period oscillations were found to be dominant by a factor of ~2.5 in amplitude during the postsolstice southern summer conditions observed in the initial Cassini interval [*Provan et al.*, 2011], while the amplitudes were found to become near-equal in the initial postequinox interval as the periods converged, due to a factor of ~2 increase in the amplitude of the northern system combined with a modest decline in amplitude of the southern system [*Andrews et al.*, 2012].

[5] It might be anticipated from these results that as seasonal conditions develop further toward northern summer at Saturn, the northern system would come to dominate the equatorial oscillations, similar to the southern system dominance during southern summer, with the periods also separating in one sense or the other similar to the latter conditions. In this paper, we examine magnetic field data from a sequence of 56 similar near-equatorial Cassini periapsis passes that took place from vernal equinox in August 2009 to November 2012, between two seasons of inclined orbits. These data thus span the first ~3.3 years of the ~8 year interval between equinox and northern summer solstice in May 2017. The large-scale study of *Andrews et al.* [2012] included the first ~1.6 years of this postequinox interval, to early 2011, which is thus extended here by a further ~1.7 years with the inclusion of data from a further 29 Cassini orbits. We demonstrate that immediately after the interval analyzed by *Andrews et al.* [2012], a major change in the behavior of the two oscillatory systems occurred, in which large abrupt changes in oscillation properties took place at ~6- to 8-month intervals, principally in the oscillation amplitudes. Three such transitions are documented. The first resulted in unexpected resumption of southern-system dominance, while the second introduced strong northern system dominance for the first time in these data, maintained at reduced levels following the third transition. Small changes in oscillation period about typical values of ~10.63 h for the northern system and ~10.69 h for the southern also occur across some of these transitions, together with modest jumps in phase. The latter values thus confirm the result of *Andrews et al.* [2012] over our extended interval that following near-convergence approximately one year after equinox in September 2010, the two periods diverged in the same sense as before, rather than crossing as suggested by *Gurnett et al.* [2010b].

2. Overview of Magnetic Field Oscillations and Theoretical Basis of the Analysis

2.1. Physical Picture

[6] The nature of the magnetospheric field oscillations determined from the above studies is sketched in Figure 1, taken from the studies by *Provan et al.* [2011] and *Andrews et al.* [2010b, 2012]. The red loops in panel (a) and the blue loops in panel (b) indicate the perturbation fields of the southern and northern systems, respectively, in their principal magnetospheric meridian planes at some instant of time. The black dashed lines indicate the near axisymmetric unperturbed magnetospheric field, with closed lines in the equatorial region (gray) and open lines extending into the tail at high latitudes (clear). The perturbation fields out of these planes can be pictured to a first approximation simply by displacing the loops directly into and out of the plane of the figure. These two field patterns then rotate independently about the planetary spin axis (Z) at the periods of the southern and northern systems, respectively.

[7] Here we focus on the equatorial perturbations, due to the near-equatorial nature of the Cassini orbits during the ~3 year interval studied here (section 3). Panels (c) and (d) of Figure 1 illustrate the perturbations in the near-equatorial quasi-dipolar region, referred to as the "core" region extending equatorially to radial distances of ~10-15 R_S, in views looking down from the north. (R_S is Saturn's 1 bar equatorial radius equal to 60,268 km.) The colored lines show the quasi-uniform perturbation field lying in the equatorial plane, while the circled dots and crosses show the north-south fields passing through the equator, as shown in panels (a) and (b). Typical perturbation field magnitudes are ~1-2 nT [*Andrews et al.*, 2010a]. The arrowed dashed circles then show the direction of rotation of these patterns with time, in the same sense as planetary rotation.

[8] In common with previous related studies, we employ spherical polar field components in a planet-centered system referenced to the northern spin and magnetic axis (Z in Figure 1). If we consider the perturbation field in panels (c) and (d) at point P in the equatorial plane, for example, it is seen that the radial components (r, positive outward) have extrema at the instant illustrated, as have the colatitudinal components (θ, positive southward), while the azimuthal components (φ, positive in the sense of planetary rotation) are zero, these conditions defining the principal meridian planes shown in panels (a) and (b). As the patterns rotate anticlockwise with time, it is seen that maxima in the φ component follow maxima in the r component one quarter cycle later in both southern and northern oscillatory systems, such that φ oscillates in lagging quadrature with r in both. It is also seen, however, that the θ component oscillates in phase with r in the southern system, but in antiphase with r in the northern system [e.g., *Andrews et al.*, 2008; *Provan et al.*, 2011], this representing the key distinction between the two systems in equatorial data.

[9] A further implication of Figure 1 is that the near-equatorial oscillations consist of the superposed perturbations of both northern and southern systems as noted in section 1, leading to varying interference effects as the oscillations go into and out of phase during their beat cycle. At the instant illustrated in the figure, the θ components in the two systems are in phase and thus add, while the r and φ components are in antiphase and will partly cancel. One half beat cycle later,
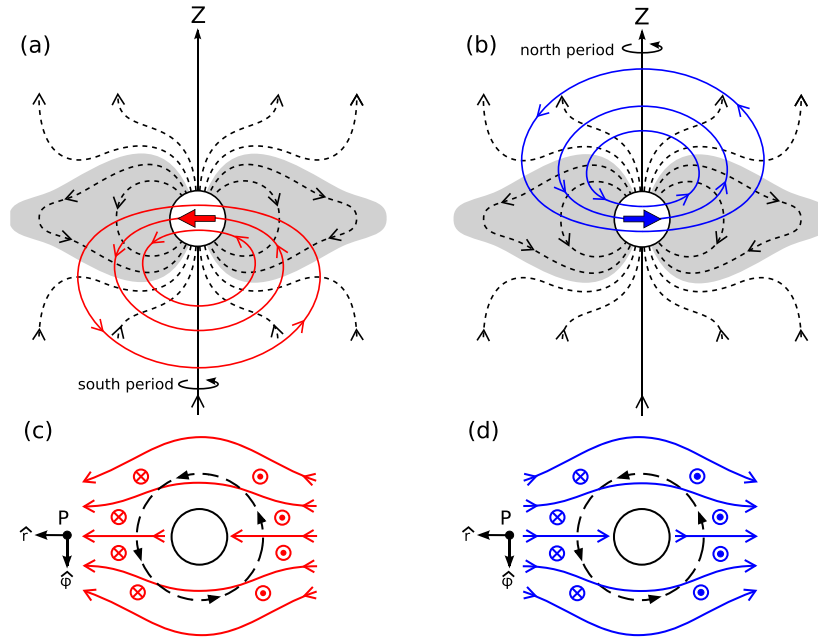
Figure 1. Sketches showing the spatial structure of (a) the southern and (b) the northern magnetic field perturbations inferred from Cassini magnetic field data. The colored lines show the perturbation fields in the principal meridian of the perturbation at any instant, where the vertical axis Z represents the spin (and magnetic) axis of the planet. The black dashed lines show the quasi-static "background" magnetospheric field. The perturbation fields out of the meridian can be obtained approximately by displacing the colored loops directly into and out of the plane of the figure. These field patterns then rotate approximately rigidly around the axis at the southern and northern periods as indicated, giving rise to magnetic field oscillations at those periods at a fixed point. Sketches of the corresponding perturbation fields in the equatorial plane are shown in panels (c) and (d), viewed from the north. The solid lines indicate the quasi-uniform equatorial field, which at the instant depicted has an extremum in the r component at point P (a maximum in (c) and a minimum in (d)) and a zero in the φ component, this condition defining the principal meridian in panels (a) and (b). The colored circled dots and crosses represent the direction of the north-south field perturbation (the θ component positive southward) at this instant, which has a maximum at point P in both cases. (From *Provan et al.* [2011] and *Andrews et al.* [2010b, 2012].)

the situation reverses, thus leading to amplitude modulations varying oppositely with beat phase for (r, φ) and for θ. Halfway between these amplitude-limiting configurations when the quasi-uniform fields are orthogonal to each other, maximal phase deviations in the combined field will occur between the (r, φ) and θ components, which also reverse sense each half-beat cycle. During the initial postsolstice southern summer interval when the northern and southern periods were ~10.6 and ~10.8 h, respectively, the beat period (whose frequency is given by the difference between the two oscillation frequencies) was ~20 days. Since this is comparable with the Cassini orbit period, and hence the cadence of the core region oscillation data, these phase effects were observed as pass-to-pass phase "jitter," first noted by *Southwood and Kivelson* [2007]. *Provan et al.* [2011] showed that these effects were due to the simultaneous presence of northern-period oscillations with amplitude ~40% of the southern oscillations, giving rise to phase variations of ±~25° about the southern phase. As the two oscillation periods converged across equinox, however, the beat period lengthened to several tens of days, allowing the beat cycle variations to be roughly followed pass-to-pass in these data [*Andrews et al.*, 2012]. In addition, the change to near-equal amplitudes in the two systems resulted in

maximal beat cycle modulations from near zero to doubling in amplitude, and ±~90° in phase, such that under this condition the combined θ component oscillates either in lagging or leading quadrature with r and hence either in-phase or antiphase with φ, rather than being in-phase or antiphase with r as in the two systems separately [*Andrews et al.*, 2012]. Analysis of these beat-phase effects then allows the separate properties of the northern and southern oscillations to be determined from the combined oscillations observed in the equatorial region.

2.2. Theoretical Analysis

[10] We now discuss the theoretical considerations underlying the oscillation data analysis in section 4 based on the above physical picture. Since we follow the analysis given previously by *Provan et al.* [2011], here specifically using the notation of *Andrews et al.* [2012], only an outline of the main assumptions will be provided, together with the principal results.

[11] We thus take the northern (*n*) and southern (*s*) system oscillations for field component *i* to be given by the real parts of the complex expressions

$$B_{in}(\varphi, t) = B_{0in}e^{j(\Phi_n(t)-\varphi-\gamma_{in})} \text{ and} \qquad (1a)$$

$$B_{is}(\varphi, t) = B_{0is}e^{j(\Phi_s(t)-\varphi-\gamma_{is})},$$

where φ is azimuth measured from noon positive toward dusk (i.e., increasing in the sense of planetary rotation), $\Phi_{n,s}(t)$ are the phase functions of the northern and southern oscillations related to the corresponding periods through

$$\tau_{n,s}(t) = \frac{360}{\left(\frac{d}{dt}\left(\Phi_{n,s}(t)\right)\right)}, \qquad (1b)$$

where the phases are expressed in degrees, and $\gamma_{in,s}$ are the fixed phase angles that define the relative phases of the oscillations in the three field components in the two systems, one of which in each system may be assigned arbitrarily. In common with previous practice, here we choose the $\Phi_{n,\,s}(t)$ functions to correspond to the phases of the r components (so that they also define the azimuths φ of the quasi-uniform fields of the two systems at any time), such that according to Figure 1 we then have

$$\gamma_{rs} = \gamma_{rn} \equiv 0° \quad \text{and} \quad \gamma_{\varphi s} = \gamma_{\varphi n} = 90° \qquad (1c,d)$$

while

$$\gamma_{\theta s} = 0° \quad \text{and} \quad \gamma_{\theta n} = 180°. \qquad (1e,f)$$

[12] For simplicity, we also assume that the amplitude ratio between the northern and southern systems $k(t)$ is independent of field component so that

$$B_{0in}(t) = k(t)B_{0is}(t) \qquad (1g)$$

for each field component i. This implies that while in general having differing amplitudes, the two perturbation systems have the same field geometry with respect to their corresponding pole as sketched in Figure 1.

[13] Summing the fields in equation (1a) into a combined oscillation $B'_{0i}(t)e^{j(\Phi'_i(t)-\varphi)}$, representing the observed oscillation for component i, and eliminating the common factor $e^{-j\varphi}$ then yields

$$B'_{0i}(t)e^{j\Phi'_i(t)} = B_{0is}\left(e^{j(\Phi_s(t)-\gamma_{is})} + ke^{j(\Phi_n(t)-\gamma_{in})}\right), \qquad (2a)$$

which may be solved for the combined phase $\Phi'_i(t)$ and amplitude $B'_{0i}(t)$. Referring to *Andrews et al.* [2012] for details, the combined oscillation phases given in terms of the deviations $\delta_{in,s} = (\Phi_{n,s} - \gamma_{in,s}) - \Phi'_i$ from either the southern or northern oscillation phases are given by

$$\delta_{r,\varphi s}(t) = \Phi_s(t) - \Phi'_r(t) = (\Phi_s(t) - 90°) - \Phi'_\varphi(t) \qquad (2b)$$

$$= \tan^{-1}\left[\frac{-k\sin\Delta\Phi}{1+k\cos\Delta\Phi}\right]$$

$$\delta_{r,\varphi n}(t) = \Phi_n(t) - \Phi'_r(t) = (\Phi_n(t) - 90°) - \Phi'_\varphi(t) \qquad (2c)$$

$$= \tan^{-1}\left[\frac{(1/k)\sin\Delta\Phi}{1+(1/k)\cos\Delta\Phi}\right]$$

$$\delta_{\theta s}(t) = \Phi_s(t) - \Phi'_\theta(t) = \tan^{-1}\left[\frac{k\sin\Delta\Phi}{1-k\cos\Delta\Phi}\right] \qquad (2d)$$

and

$$\delta_{\theta n}(t) = (\Phi_n(t) - 180°) - \Phi'_\theta(t) = \tan^{-1}\left[\frac{-(1/k)\sin\Delta\Phi}{1-(1/k)\cos\Delta\Phi}\right]. \qquad (2e)$$

[14] The difference phases between the combined components are correspondingly given by

$$\Delta\psi_{\varphi-r} = \Phi'_r(t) - \Phi'_\varphi(t) = (\delta_{\varphi n,s}(t) + 90°) - \delta_{rn,s}(t) = 90°, \qquad (2f)$$

and

$$\begin{aligned}\Delta\psi_{r-\theta} &= \Phi'_\theta(t) - \Phi'_r(t) = \Phi'_\theta(t) - (\Phi'_\varphi(t) + 90°) \\ &= \delta_{r,\varphi s}(t) - \delta_{\theta s}(t) = \delta_{r,\varphi n}(t) - \delta_{\theta n}(t) - 180° \\ &= -\tan^{-1}\left[\frac{2k\sin\Delta\Phi}{1-k^2}\right].\end{aligned} \qquad (2g)$$

[15] In these expressions, $\Delta\Phi(t)$ is the beat phase given by

$$\Delta\Phi(t) = \Phi_n(t) - \Phi_s(t), \qquad (2h)$$

with corresponding beat period $\tau_B(t)$ given by

$$\tau_B(t) = \frac{\tau_s\tau_n}{(\tau_s - \tau_n)} = \frac{360}{\left(\frac{d}{dt}\left(\Delta\Phi(t)\right)\right)}, \qquad (2i)$$

where the phase angles are again in degrees. We note that in all the above arctangent functions, the signs of the numerator and denominator are taken separately to define the value of the angle over the full 360° range. The combined oscillation amplitudes are given by

$$\begin{aligned}B'_{0r,\varphi}(t) &= B_{0r,\varphi s}\sqrt{1 + k^2 + 2k\cos\Delta\Phi} \\ &= B_{0r,\varphi n}\sqrt{1 + (1/k)^2 + 2(1/k)\cos\Delta\Phi},\end{aligned} \qquad (2j)$$

and

$$\begin{aligned}B'_{0\theta}(t) &= B_{0\theta s}\sqrt{1 + k^2 - 2k\cos\Delta\Phi} \\ &= B_{0\theta n}\sqrt{1 + (1/k)^2 - 2(1/k)\cos\Delta\Phi}.\end{aligned} \qquad (2k)$$

2.3. Implications of Theoretical Results

[16] The implications of the above results are illustrated in Figure 2 using vector diagrams in the Argand plane combined with plots showing how the phase and amplitude of the combined oscillations vary with the beat phase $\Delta\Phi$. Panel (a) corresponds to the case with k less than unity, specifically $k = 0.5$, such that the southern system amplitudes are twice the northern. In the Argand diagram, we then de-spin the southern oscillation vectors B_{rs} and $B_{\theta s}$ by rotating anticlockwise at the angular frequency corresponding
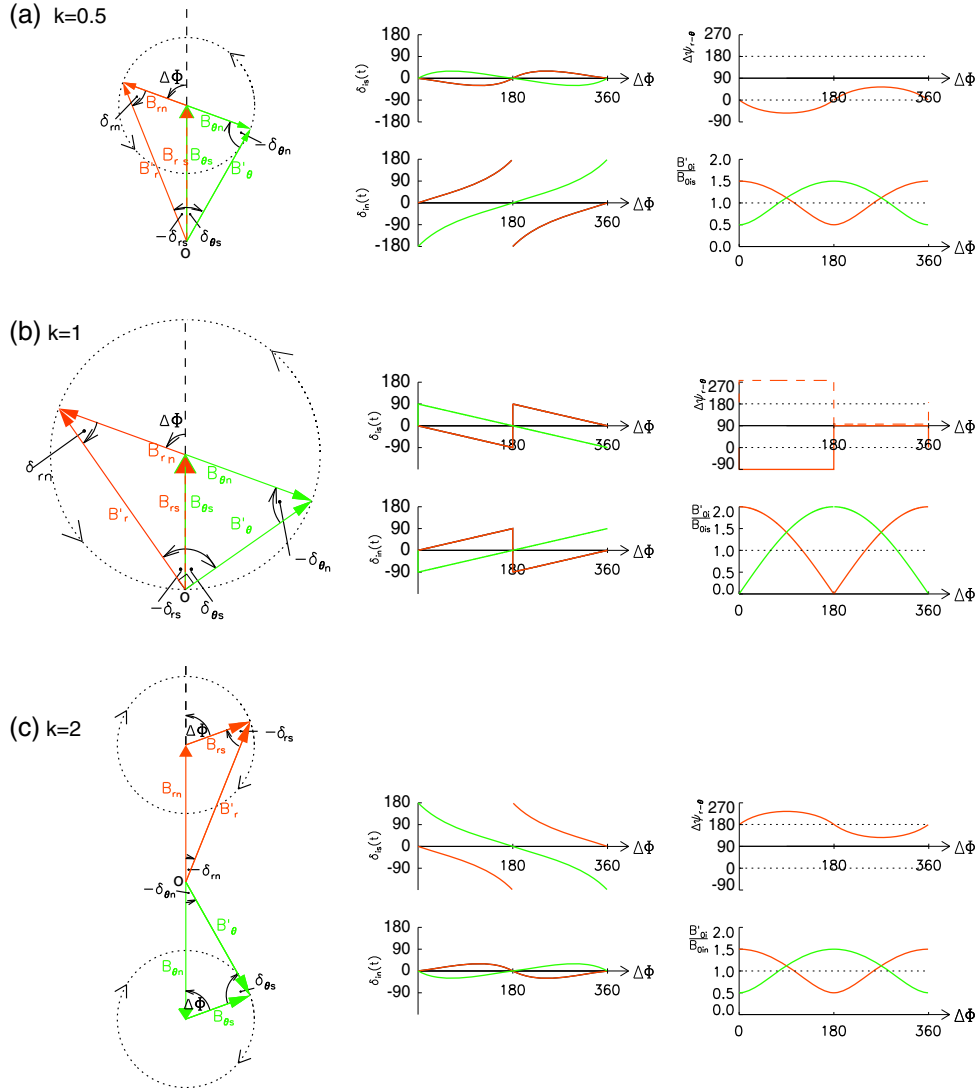
Figure 2. Vector diagrams in the Argand plane illustrating the result of superposition of southern and northern system oscillations in the equatorial magnetosphere, specifically for the r (red) and θ (green) field components, together with plots showing the corresponding phase and amplitude variations of the combined oscillations with beat phase $\Delta\Phi$. Specifically, the plots show the variation with $\Delta\Phi$ of the oscillation phases for each field component i with respect to both the southern and northern phases, δ_{is} and δ_{in}, respectively, as shown for each component in the vector diagram, the phase difference $\Delta\psi_{r-\theta}$ between the combined r and θ component oscillations equal to $\delta_{rs} - \delta_{\theta s} = \delta_{rn} - \delta_{\theta n} - 180°$, and the variation of the normalized amplitudes. Panels (a), (b), and (c) are for north/south amplitude ratios of $k = 0.5$, 1, and 2, corresponding to southern dominance, equal amplitudes, and northern dominance, respectively.

to $\Phi_s(t)$ and draw both fixed vertically from origin O forming the red-green dashed line, the parallel directions indicating in-phase oscillations of these two components in the southern system. We also normalize these vectors to unit length. The vectors representing the northern oscillations B_{rn} (red) and $B_{\theta n}$ (green) are drawn from the tips of these vectors, at beat phase angle $\Delta\Phi$ for B_{rn}, and in the antiparallel direction for $B_{\theta n}$, representing antiphase oscillations of these components in the northern system. The normalized length of both northern vectors is then k, equal to 0.5 in this case. The combined oscillations given by equation (2a) are then shown by the sums of the southern- and northern-system vectors, forming combined oscillation vectors B'_r (red) and B'_θ (green).

The length of these vectors represent the normalized amplitudes of the combined oscillations B'_{0r} and $B'_{0\theta}$ given by equations (2j) and (2k), while the angles relative to the northern and southern vectors show the phase deviations $\delta_{rn,s}$ and $\delta_{\theta n,s}$ given by equations (2b)–(2e). We note that the corresponding diagram for the φ component is identical to that for r at any instant but rotated 90° clockwise and hence is not shown here.

[17] With increasing time, the northern vectors rotate with the beat period corresponding to $\Delta\Phi(t)$, anticlockwise if the southern period is longer than the northern as indicated by the arrowed black dotted circle in the Argand diagram in panel (a) of Figure 2, such that the phase and amplitude of

the combined oscillations undergo cyclic modulations at the beat period. These are plotted on the right side of panel (a), where the plots in the first column show the phase deviation δ_{is} relative to the southern oscillation phase for r (red) and θ (green) (equations (2b) and (2d)) and the phase deviations δ_{in} relative to the northern oscillation phase in the same format (equations (2c) and (2e)). The plots in the second column show the phase difference between these two field components $\Delta\psi_{r-\theta}$ (equation (2g)), and the amplitudes normalized to the southern oscillation amplitudes for r (red) and θ (green) (equations (2j) and (2k)). The phase deviations with respect to the southern phase vary with $\Delta\Phi$ near-sinusoidally about zero under these conditions, while the deviations with respect to the northern phase vary over the full 360º range. Extremal values of δ_{is} are $\pm\sin^{-1}(k)$ which occur when the summed vectors in the Argand plane are tangent to the dashed circle, at the two beat phase angles $\Delta\Phi=\cos^{-1}(-k)$ for r (and φ) and $\Delta\Phi=\cos^{-1}(k)$ for θ. Phase difference $\Delta\psi_{r-\theta}$ also varies near-sinusoidally about zero, with extremal values $\mp\sin^{-1}(2k/1+k^2)$ occurring at $\Delta\Phi=90°$ and 270º when the quasi-uniform fields of the two systems are orthogonal. Extremal values of the normalized amplitudes $(1+k)$ and $(1-k)$ occur at $\Delta\Phi=0°$ and 180º, respectively, for r, and vice versa for θ. These results are in accord with the qualitative discussion given in section 2.1.

[18] Panel (b) of Figure 2 corresponds to the limiting case of equal northern and southern amplitudes, i.e., $k=1$. The Argand plane diagram shows that under this condition, the combined r and θ vectors are exactly orthogonal for all $\Delta\Phi$, such that these components oscillate in quadrature as indicated in section 2.1. The r oscillations lead θ during the half beat cycle $0°\leq\Delta\Phi\leq180°$ (illustrated in the figure), such that θ then oscillates in phase with φ, while r lags θ during the remaining half beat cycle $180°\leq\Delta\Phi\leq360°$, such that θ then oscillates in antiphase with φ. The phase differences with respect to the southern phase δ_{is} shown in the first column on the right fall linearly with time between +90º and -90º, switching abruptly between these values at $\Delta\Phi=180°$ for r and at $\Delta\Phi=0°$ for θ. Similarly, the phase differences with respect to the northern phase rise linearly with time between -90º and +90º, switching abruptly between these values at the same beat phases. Thus, for equal amplitudes, the phases of the combined oscillations raster linearly between ±90º about both the southern and the northern oscillation phases (i.e., through one half of the full 360º range), one falling and the other rising with the beat phase. As will be discussed in section 4, this dual clustering of the phase values about both southern and northern phases forms the basis of the method developed by *Andrews et al.* [2012] to obtain both the northern and southern phases from such data. The phase difference $\Delta\psi_{r-\theta}$ in the second column then varies as a "square wave" between -90º and +90º as shown by the solid line, corresponding to leading and lagging quadrature as noted above or equivalently (modulo-360º) between +270º and +90º as shown by the dashed line. This behavior can thus be regarded as either a variation of ±90º about the southern value of 0º or about the northern value of 180º, thus forming a bridge between the behavior for $k<1$ shown in panel (a) and that for $k>1$ shown in panel (c). We also note that the 180º switches in phase difference occur sequentially at the times when the amplitude of one of the combined field components reaches zero, at $\Delta\Phi=0°$ (modulo 360º) for θ and 180º for r (and φ).

[19] Panel (c) of Figure 2 corresponds to the case with k greater than unity, specifically $k=2$, such that the northern oscillation amplitude is twice the southern. We then de-spin the northern vectors B_{rn} and $B_{\theta n}$ in the Argand diagram, drawn normalized in opposite directions from origin O, indicating antiphase oscillations of these components in the northern system. The parallel vectors representing the in-phase southern oscillations B_{rs} and $B_{\theta s}$ are then drawn from the tips of these vectors at angle $\Delta\Phi$ with normalized lengths $1/k$ equal to 0.5 in this case, with the combined oscillations being shown by the vector sums B'_r and B'_θ. With increasing time, the southern vectors rotate with the beat period corresponding to $\Delta\Phi(t)$, as indicated by the arrowed black dotted circles, clockwise as shown if the southern period remains longer than the northern, leading to the phase and amplitude variations shown on the right. The phase deviations with respect to the southern phase now vary with $\Delta\Phi$ over the full 360º range, while the deviations with respect to the northern phase vary near-sinusoidally about zero, in the same manner as the opposite deviations for $k=0.5$, except for a change in sign. Correspondingly, the phase difference $\Delta\psi_{r-\theta}$ now varies with the beat period about 180º in the same way but in the opposite sense as the oscillations about 0º for $k=0.5$. The amplitude variations normalized to the northern amplitudes, as shown, are then identical to the case for $k=0.5$.

[20] We recall that given the definition of the beat phase in equation (2h), $\Delta\Phi(t)$ increases with time if the southern period is longer than the northern and decreases with time if the northern is longer than the southern. It is then notable in Figure 2 that a switch in the period of the two systems, though leading to identical beat periods, would be readily identifiable in the opposite temporal behaviors of the phase deviations about the northern and southern phases and in the opposite temporal variations of the combined amplitudes relative to the phase differences.

2.4. Relation to Cassini Phase Data

[21] We now relate the theoretical analysis to the phases and amplitudes determined from Cassini data. As will be discussed in section 3, the filtered residual data for each field component i are least-squares fitted for each periapsis pass to the "$m=1$" rotating function

$$B_i(\varphi, t) = B_{0i}\cos\big(\Phi_g(t) - \varphi - \psi_i\big), \qquad (3a)$$

where $\Phi_g(t)$ is some suitably chosen "guide" phase whose related period is close to the period of the oscillations, and φ is again azimuth measured from noon positive toward dusk. The amplitude B_{0i} and relative phase ψ_i (modulo 360°) of the observed oscillations are determined from the fit. In this paper, we have chosen the guide phase to correspond to a fixed guide period τ_g given by

$$\Phi_g(t) = \frac{360t}{\tau_g}\ \text{deg}, \qquad (3b)$$

where, in common with earlier studies, $t=0$ corresponds to 00 UT on 1 January 2004, and we have made the arbitrary choice $\Phi_g(0)=0\,\text{deg}$. The differences in the phases ψ_i between the three field components, written for components j and k as

$$\Delta\psi_{j-k} = \psi_j - \psi_k, \qquad (3c)$$

indicate the polarization of the oscillations, while the variation of these phases from pass to pass is governed by both the difference between the field oscillation period and the guide phase period and other physical effects that are present such as the beat effects discussed in sections 2.2 and 2.3. Specifically, equations (3a) and (2a) show that $\Phi'_i(t) = \Phi_g(t) - \psi_i(t)$ where $\psi_i(t)$ represents the phases determined from pass to pass over time, given in terms of the beat-phase model by

$$\psi_i(t) = \Phi_g(t) - \Phi'_i(t) = \left(\Phi_g(t) - (\Phi_s(t) - \gamma_{is})\right) + \delta_{is}(t) \quad (3d)$$

$$= \left(\Phi_g(t) - (\Phi_n(t) - \gamma_{in})\right) + \delta_{in}(t). \qquad (3e)$$

[22] The first terms within the brackets on the right hand side vary smoothly with time depending on the difference between the guide period and the southern or northern system period, while the second vary with the beat period as given by equations (2b)-(2e). Independent of the choice of guide phase, the models of the phase differences $\Delta\psi_{j-k}$ are then given by equations (2f) and (2e), where the notation of equation (3c) was already anticipated.

3. Magnetic Oscillation Data Overview

3.1. Spacecraft Orbit

[23] We analyze the relatively homogeneous data set obtained on 56 near-equatorial Cassini orbits with periapsides in the dawn sector that took place between the second high-latitude mission phase ending in mid-2009 and the third starting in late 2012. The specific Cassini orbit "revolutions" (Revs) concerned, defined from apoapsis to apoapsis, are Revs 116 to 175, spanning the initial ~3.3 years of Saturn northern spring between equinox in August 2009 and November 2012. We note that the previous analysis presented by *Andrews et al.* [2012] extended to Rev 146 in March 2011, thus encompassing the first ~1.6 years of the postequinox interval. Here we newly examine data from 29 subsequent Revs occurring over the following ~1.7 years to November 2012 and relate the results to those of the earlier postequinox interval.

[24] Example orbits from this data set are shown in Figure 3, color-coded by Rev number as shown at the top of the figure. In panel (a), we show orbit projections onto Saturn's equatorial plane, where the Z axis (out of the figure) is aligned with Saturn's rotation and magnetic axis, the X-Z plane contains the Sun, and Y completes the right-hand system directed from dawn to dusk. The temporal evolution of each orbit is anticlockwise, in the same sense as planetary rotation. For purposes of scale, the black dot-dashed and dashed lines show cuts through the magnetopause and bow shock for a typical solar wind dynamic pressure of 0.03 nPa according to the models of *Kanani et al.* [2010] and *Masters et al.* [2008], respectively, while the black dotted circle indicates the equatorial boundary of the quasi-dipolar "core" region of the magnetosphere, taken here to extend to 12 R_S in the equatorial plane. It can be seen that the orbit character varies only modestly over the three-year interval, with apoapsis typically at ~40-50 R_S rotating from

(a) Revs
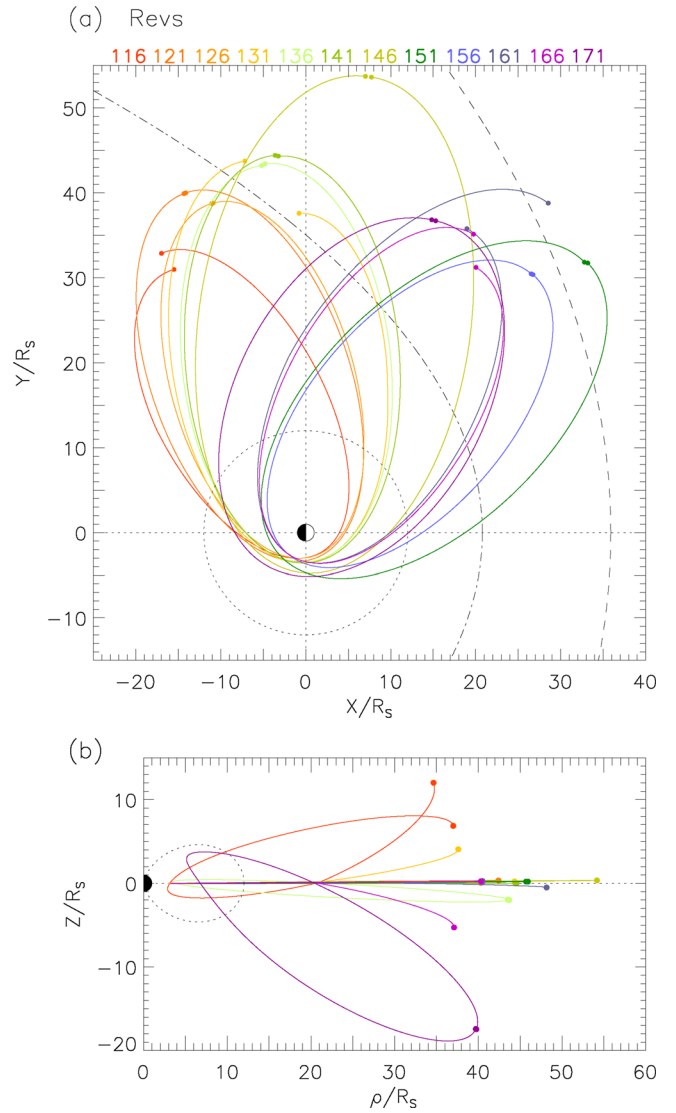
Figure 3. Representative Cassini orbits plotted from apoapsis to apoapsis, color-coded by Rev number as shown at the top of the figure. In panel (a), the orbits are projected onto Saturn's equatorial plane using KSMAG coordinates, where the Z axis is aligned with Saturn's magnetic and rotation axis, the X-Z plane contains the Sun, and Y completes the right-handed system. Temporal evolution of the orbits is anticlockwise, in the same sense as planetary rotation. The black dot-dashed and dashed curves show equatorial cuts through the magnetopause and bow shock for a typical dynamic pressure of 0.03 nPa, according to the models of *Kanani et al.* [2010] and *Masters et al.* [2008], respectively. These boundaries are defined in kronian solar magnetospheric coordinates and are shown specifically for $t = 2500$ days near the center time of the interval, though the variation over the interval is small. The black dotted circle shows the 12 R_S equatorial limit taken here for the quasi-dipolar core region of the magnetosphere. Panel (b) shows the same orbits projected onto a meridian plane using ρ-Z cylindrical coordinates. Temporal evolution of the tilted orbits at the beginning and end of the sequence is clockwise. The black dotted curve shows the $L = 12$ dipole flux shell, defining the core region from which data are employed in this study.

postdusk to predusk (~19 h to ~15 h local time (LT)), while periapsis typically at ~3-6 R_S correspondingly rotates from postdawn to predawn (~7 h to ~3 h LT).

[25] Panel (b) of Figure 3 shows the same orbits projected onto the meridian plane using ρ-Z cylindrical coordinates, where $\rho = \sqrt{X^2 + Y^2}$ is the perpendicular distance from the Z axis. This illustrates the closely equatorial nature of the central set of Revs, together with the orbit evolution from higher latitudes toward the equator in the initial Revs and from the equator to higher latitudes in the final Revs. The trajectories are traversed clockwise in both the latter cases. The black dotted line indicates the $L = 12$ dipole flux shell, defining the trajectory segments from which data were employed in this study.

3.2. Postequinox Core Region Oscillations

[26] We first discuss the nature of the core region field oscillations observed on individual periapsis passes, illustrating the method employed to determine the phase and amplitude data and the varying properties of the oscillations during the interval studied. In particular, we examine the phase difference between the (r, φ) and θ component oscillations since it is evident from section 2.3 that this provides a prime diagnostic of the nature of the oscillations observed. In plots (a) and (b) of Figure 4, we show magnetic field data from two passes during the early postequinox interval studied previously by *Andrews et al.* [2012], specifically Revs 121 and 123. Each plot shows four days of data centered on periapsis, which occurred on days 325 and 360 of 2009, respectively.
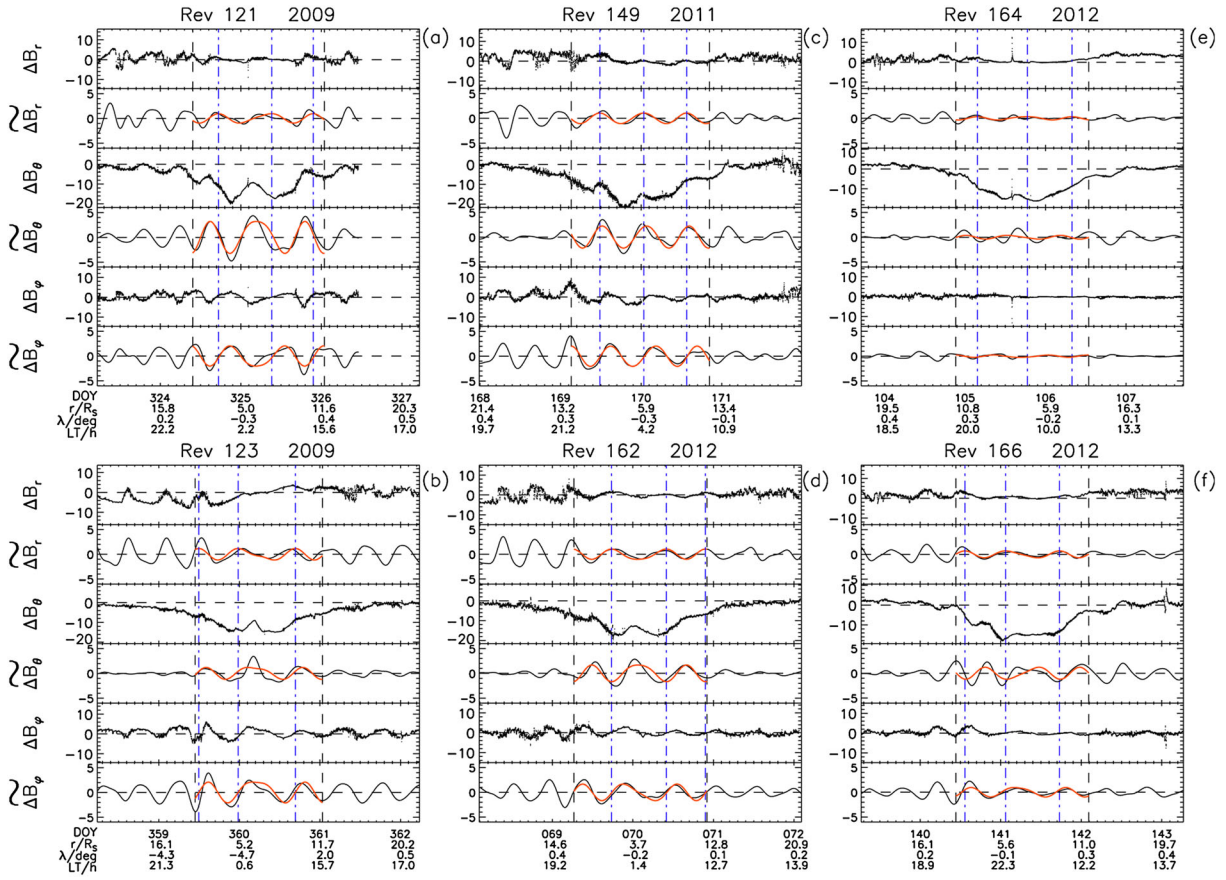
Figure 4. Periapsis pass data from six Cassini Revs illustrating the varying behavior observed during the study interval. Each plot shows four days of data centered on periapsis, where from top to bottom, we show residual and band-pass filtered magnetic data for the r, θ, and φ field components. The residual data (ΔB_i for field component i) have the Cassini SOI internal planetary field model subtracted, while the filtered residual data ($\overline{\Delta B}_i$ for field component i) have been band-pass filtered between 5 and 20 h to extract the planetary-period signal. All field values are in nT. The Rev number and year are given at the top of each plot, while values at the foot indicate the start time of each day of year (DOY), together with the spacecraft radial distance (R_S), latitude (deg), and LT (h). The interval between the pair of vertical black dashed lines corresponds to the core region defined by dipole $L \le 12$, inside which the filtered residual data have been least-squares fitted to the model field given by equation (3a) using a guide phase corresponding to a fixed period of 10.68 h as given by equation (3b). The fitted model is shown by the red curves. The vertical blue dot-dashed lines indicate the position of the maxima in the fitted r component, allowing the relative phases of the two other components to be readily examined. Plots (a) to (f) show data for Revs 121, 123, 149, 162, 164, and 166, respectively, as discussed in section 3.2.

Rev number and year are given at the top of each plot, while day of year (DOY) and spacecraft radial distance, latitude, and LT are given at the start of each day at the bottom. Pairs of panels in each plot show residual (ΔB_i for field component i) and band-pass filtered ($\overline{\Delta B_i}$) data for each spherical polar field component as indicated, with all field values being given in nT. The residual data have the Cassini SOI model internal planetary field subtracted [*Dougherty et al.*, 2005], but since the model field is axisymmetric with zero φ component, the B_φ data in each plot is that directly measured. Field oscillations near the planetary period at few-nT amplitude are evident throughout both passes, superposed in the case of the residual θ component on a large more slowly varying negative perturbation due to the ring current. To isolate the planetary period signals, these residual data have been band-pass filtered between 5 and 20 h using a standard Lanczos filter, the filtered data being shown in the panels beneath the residual data for each field component.

[27] The core region intervals in Figure 4 are those between the black vertical dashed lines in each plot, defined in common with previous studies as the region with dipole $L \leq 12$. The filtered residual data for each component i in these intervals are then least-squares fitted to equation (3a) using a guide phase corresponding to a fixed period $\tau_g = 10.68h$, close to the mean period of the northern and southern systems throughout, thus yielding values of the amplitude B_{0i} and relative phase ψ_i (modulo 360°) for each pass. The fitted model curves are shown by the red lines in the filtered data panels, while vertical blue dot-dashed lines have been drawn through the peaks in the fitted r component so that the phase relations with the other components can be readily examined.

[28] It is first seen that the oscillations in the φ component are close to lagging quadrature with those in r in both plots (a) and (b), such that the peaks in φ occur one quarter cycle later than those in r as indicated in section 2. Quantitatively, the phase difference $\Delta\psi_{\varphi-r}$ of the fits is 100° for Rev 121 and 90° for Rev 123. Physically meaningful uncertainties in these values are difficult to assign on an individual basis, but empirical results presented by *Andrews et al.* [2012] and in section 3.3 suggest values $\pm \sim 10°$. Examination of the θ component oscillations then shows that to a good approximation, they are in leading quadrature with r for Rev 121 and hence in antiphase with φ, while being in lagging quadrature with r for Rev 123 and hence in phase with φ. Specifically, the phase differences $\Delta\psi_{r-\theta}$ are 78° for Rev 121 and -69° for Rev 123. As discussed in section 2, these polarizations are indicative of the superposition of northern and southern systems with near-equal amplitudes, as previously reported for this interval by *Andrews et al.* [2012].

[29] Plots (c) and (d) of Figure 4 show data from two later passes beyond those studied by *Andrews et al.* [2012], specifically Revs 149 and 162 with periapses on days 169 of 2011 and 70 of 2012, respectively. In both cases, the φ component again oscillates in near-lagging quadrature with r, with phase differences $\Delta\psi_{\varphi-r}$ of 95° for Rev 149 and 94° for Rev 162. However, on Rev 149, the θ component oscillates approximately in-phase with r with $\Delta\psi_{r-\theta}$ of -22°, unexpectedly indicative of resumed southern system dominance, while on Rev 162, the θ component oscillates in antiphase with r with $\Delta\psi_{r-\theta}$ of 179°, newly indicative of northern system dominance in these data.

[30] Plots (e) and (f) of Figure 4 show data from the later interval examined here, for Revs 164 and 166 with periapses on days 105 and 141 of 2012, respectively. Rev 164 is very unusual in showing only small oscillations to be present in all three field components, with fitted amplitudes ~0.2-0.4 nT compared with typical values ~1-3 nT in the other plots in Figure 4. Small amplitudes are occasionally present in the earlier postequinox data studied by *Andrews et al.* [2012] but then occur either in (r, φ) and not in θ or in θ and not in (r, φ), due to the beat phase effects discussed in section 2. In the case of Rev 164, the amplitudes in all components are sufficiently small that the phase data are considered unreliable (see section 3.3) and are not employed in further analysis. The data for Rev 166 then show significant recovery of the amplitudes toward more usual values, with the φ oscillations being roughly in quadrature with r, $\Delta\psi_{\varphi-r}$ being 58°, while θ is again in antiphase with r, $\Delta\psi_{r-\theta}$ being 172°, thus again indicating northern system dominance.

3.3. Overview of Phase Difference Data

[31] The examples in Figure 4 demonstrate an unanticipated variability in the oscillation properties during the postequinox interval, which we now examine in greater detail. In Figure 5, we provide an overview of the phase difference data, plotted versus time over the study interval, together with information on the position of spacecraft periapsis to examine whether changes in oscillation properties could be related to changes in orbit coverage. Panels (a) and (b) thus show the radial distance and LT of Cassini periapsis, respectively, while panel (c) shows $\Delta\psi_{\varphi-r}$ and (d) both $\Delta\psi_{r-\theta}$ and $\Delta\psi_{\varphi-\theta}-90°$ as discussed below. The time of periapsis on each Rev is shown at the top of the figure, numbered every fourth Rev, together with year boundary markers. As indicated above, the data span a ~3.3-year interval from near vernal equinox in August 2009 (also marked at the top of the figure) to November 2012.

[32] Data are not shown in Figure 5 for Revs 118, 140, 160, and 172, for which extended data gaps resulted in no core data being recorded, while for all other Revs near-continuous data spanning at least one oscillation period were recorded within the core, in principle allowing phases to be determined. Linear interpolation was employed across field spikes related to moon fly-bys (e.g., plot (e) of Figure 4 on day 2012/105) and across data gaps short compared with the oscillation period. Phase values have been rejected if the fit between the data and model equation (3a) is poor, indicative of competing effects contributing power to the filter band, and if the fitted amplitude is small, for similar reasons. Empirically determined limits are RMS fit deviations that are a factor of more than 1.4 times the amplitude (i.e., a ratio modestly larger than unity) and amplitudes less than 0.35 nT, these representing marginally more stringent limits than employed previously by *Andrews et al.* [2012]. We note, however, that the amplitude data for these cases are retained, since they represent indicative upper limits in cases where the amplitude is small. In addition, r component data (both phase and amplitude) were rejected for a small number of tilted orbits (Revs 116, 124, and 170-175) in which a rapid switch in sign of the radial field near periapsis resulting from crossing through the ring current also contributed significant power to the filter band (see the study by *Andrews et al.* [2008]). Overall, these conditions led to the rejection of less than 10% of the phase data.
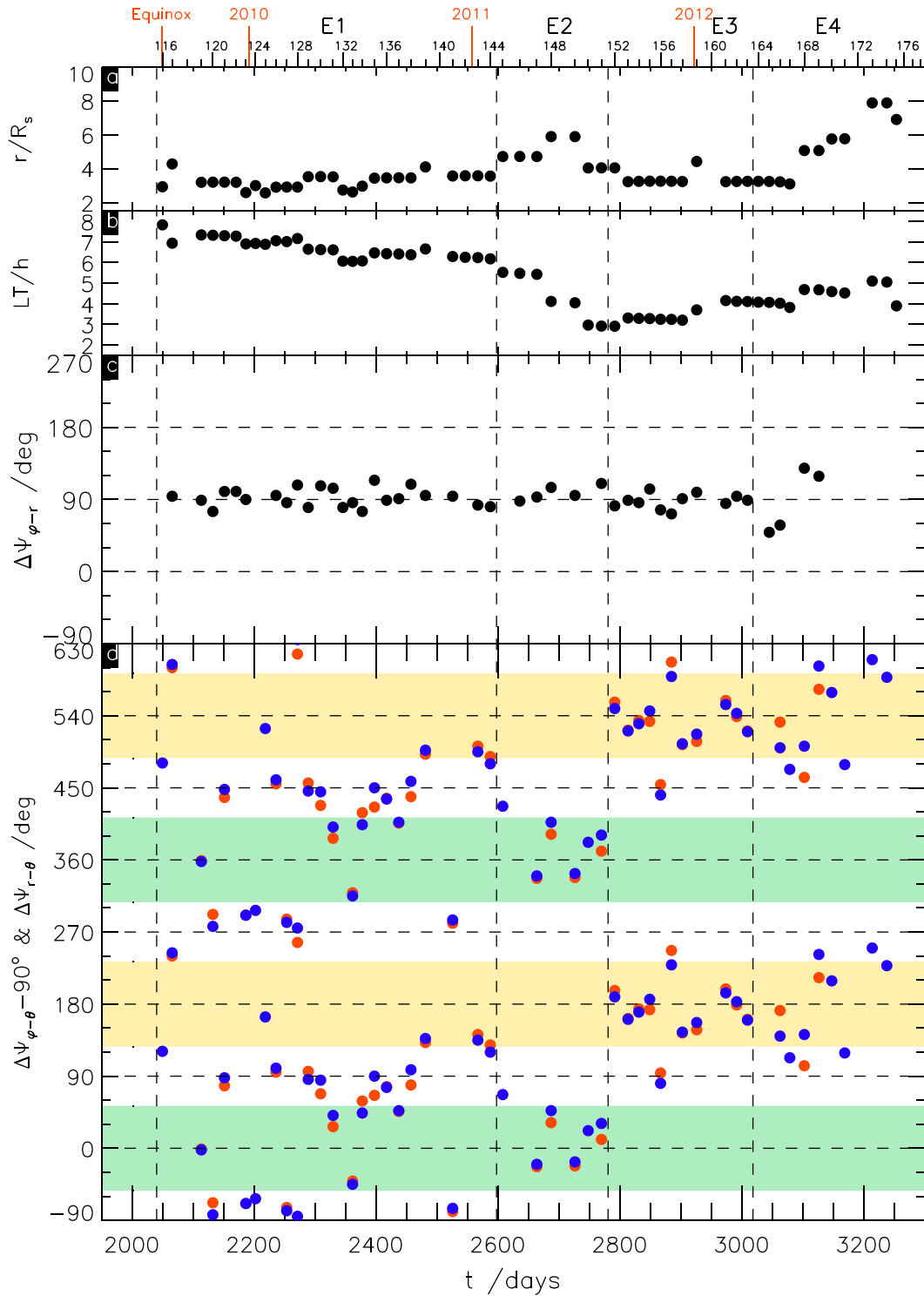
Figure 5. Overview of phase difference and orbit parameter data over the ~3.3-year study interval from near equinox in August 2009 to November 2012 spanning Revs 116 to 175. The time of periapsis on each Rev is shown at the top of the figure, numbered every fourth Rev (black), together with year boundary markers and the time of vernal equinox (red). Interval identifiers E1-E4 are also shown, delimited by the vertical black dashed lines in the plot. Panel (a) shows the radial distance of periapsis on each Rev (R_S), (b) the LT of periapsis (hours), (c) the phase difference $\Delta\psi_{\varphi-r}$ (deg) (black solid circles), and (d) phase differences $\Delta\psi_{r-\theta}$ (red solid circles) and $\Delta\psi_{\varphi-\theta} - 90°$ (blue solid circles). In panel (d), two cycles of phase are shown on the vertical axis, with each data point being plotted twice. The colored horizontal stripes in panel (d) show phase bands indicating either southern (green) or northern (yellow) system dominance, specifically corresponding to amplitude ratios $k \le 0.5$ and $k \ge 2$, respectively, while data in the white bands indicate amplitude ratios nearer to unity between these limits.

[33] We first examine the $\Delta\psi_{\varphi-r}$ data shown by black solid circles in panel (c) of Figure 5. The values are close to 90º essentially throughout, such that φ is in lagging quadrature with r, consistent with a rotating quasi-uniform equatorial field as discussed in section 2. The main exceptions are for Revs 165-169 at the end of the interval, where larger deviations are evident. With the exclusion of these values, the mean and standard deviation of these data are 92.0º and 10.3º, respectively. (Definitions of these quantities appropriate to modulo 360º angular data are given in section A.1 of Appendix A.) The standard deviation is thus consistent with uncertainties in the phase differences of $\pm \sim 10º$ as mentioned in section 3.2, though this has the character of an upper limit since some of the variability could be physical.

[34] Given the near-constancy of $\Delta\psi_{\varphi-r} \simeq 90°$ for most of these data, the phase differences $\Delta\psi_{r-\theta}$ and $\Delta\psi_{\varphi-\theta} - 90°$ can be considered to give essentially equivalent measures of the phase relation between the (r, φ) oscillations associated with the quasi-uniform field and the north-south field θ, specifically of the phase between the r and θ components. In panel (d) of Figure 5, we thus plot both $\Delta\psi_{r-\theta}$ (red solid circles) and $\Delta\psi_{\varphi-\theta} - 90°$ (blue solid circles), as available. Two cycles of phase are employed on the vertical axis to help display the continuity of the data, with each modulo 360º data point being plotted twice. The horizontal colored bands indicate the phase difference ranges that would contain these data if the oscillations are dominated by either the southern (green bands) or northern (yellow bands) systems, it being recalled from section 2.3 that for southern system dominance $\Delta\psi_{r-\theta}$ and $\Delta\psi_{\varphi-\theta}$ 90° vary with the beat cycle about the southern system value 0º (modulo 360º), while for northern system dominance, they similarly vary about the northern system value 180º (modulo 360º). Quantitatively, the range of variation about these values is given by $\pm \sin^{-1}(2k/(1+k^2))$, where k is the north/south amplitude ratio. The green bands show the range that would contain the phase differences for $k \leq 0.5$, i.e., for southern amplitudes more than twice the northern, extending $\pm 53º$ about 0º (modulo 360º), while the yellow bands similarly show the range that would contain the data for $k \geq 2$, i.e., for northern amplitudes more than twice the southern, extending through the same range about 180º (modulo 360º). Data lying in the $\pm 37º$ white intervals between the colored bands then indicate amplitude ratios in the range $0.5 \leq k \leq 2$ about unity, in which case the extremal phase differences switch between the band centered on 90º (modulo 360º) and that centered on 270º (modulo 360º) each half beat cycle.

[35] These data show that in the interval spanning Revs 116-144, the phase differences typically lie within the white bands, indicative of amplitude ratios near unity, as reported by *Andrews et al.* [2012]. Plots (a) and (b) of Figure 4 show data for two of these passes, Revs 121 and 123 from November and December 2009, one lying in each of the two bands. For future reference, we term this interval E1 as indicated at the top of Figure 5 (continuing to employ the orbit-type interval nomenclature introduced by *Andrews et al.* [2012]), which begins at $t = 2040$ days (2 August 2009) at the start of the near-equatorial orbits examined here, and is taken to end, for definiteness, mid-way between the periapsis times of Revs 144 and 145 at $t = 2597$ days (10 February 2011). These times are indicated by the first and second vertical dashed lines in the figure.

[36] Starting with Rev 145, there then follows a series of passes where the phase difference values lie continuously

within or near the green band, unexpectedly indicative of resumed southern system dominance, similar to the southern summer data from the initial Cassini equatorial-orbit intervals in 2004–2007 (intervals A and C in the nomenclature of *Andrews et al.* [2012]). Plot (c) of Figure 4 shows data for one of these passes, for Rev 149 in June 2011. These conditions persisted for ~180 days (~6 months) encompassing Revs 145–151 that we term interval E2, ending two years after equinox at $t = 2780$ days (12 August 2011) shown by the third vertical dashed line.

[37] Beginning at Rev 152, there then follows an abrupt transition to values lying continuously within or near the yellow band indicating northern system dominance, with phase differences varying continually about 180º (modulo 360º) for the first time in these data. These conditions are exemplified by Rev 162 in March 2012 in plot (d) of Figure 4 and continue for ~240 days (~8 months) encompassing Revs 152–163 that we term E3, ending at $t = 3018$ days (5 April 2012) shown by the fourth vertical dashed line. We note that the values for Revs 156 and 157 ($t \simeq 2860 - 2890$ days) again move near or into the two white bands, indicative of k being briefly closer to unity in this interval, but here we have avoided further subdivision of these data.

[38] \Significant new behavior is again indicated starting at Rev 164 in April 2012, where initially the amplitudes are sufficiently low that phases are not well determined, as shown in plot (e) of Figure 4. The phase difference values from later Revs, however, are seen to be well scattered about 180º within and just outside the yellow band, indicative of continued northern dominance but generally to a lesser degree than for interval E3. This is illustrated in plot (f) of Figure 4 for Rev 166 in May 2012. These conditions, defining interval E4, continue for at least ~240 days (~8 months) encompassing Revs 164–175 to the end of the data included in this study. The latter corresponds to apoapsis at the end of Rev 175 at $t = 3259$ days (3 December 2012), though the periapsis pass for this Rev actually occurred at the end of November 2012.

[39] In addition to these major changes, we also note from panel (d) of Figure 5 that an earlier episode of relative southern dominance occurred in E1 during Revs 131–137 ($t \simeq 2320 - 2440$ days, May 2010), as well as relative northern dominance during Revs 139–144 ($t \simeq 2470 - 2590$ days, October 2010). Taken together with the later variations, these data demonstrate a far from monotonic seasonal transition from southern to northern system dominance. In addition, the variation in the later data is far from smooth, with major changes occurring abruptly from one pass to the next over intervals as short as a few tens of days, followed by relatively stable behavior lasting ~200 days. Comparison with the orbital data at the top of Figure 5 indicates no evident correspondence between these major changes and changes in orbital coverage of the spacecraft. In particular, no changes in orbit occurred across the boundary between E2 and E3, nor between E3 and E4, such that temporal variations in the oscillation properties themselves are clearly implicated.

4. Determination of Southern and Northern Oscillation Phases and Amplitudes

[40] In this section, the individual properties of the northern and southern systems are derived from the observed combined oscillation data using techniques tailored to the nature of the

data but principally using the method developed by *Andrews et al.* [2012], which we start by outlining.

4.1. The Method of *Andrews et al.* [2012]

[41] In this method, the phase data (the ψ_i values) for each field component for each pass are plotted in two different formats, one appropriate to oscillations dominated by the southern system, termed "S-format," the other appropriate to oscillations dominated by the northern system, termed "N-format." In S-format, the r and θ component phase data are plotted as measured, while 90º is subtracted from the φ component values, such that for oscillations dominated by the southern system, all the phase values lie on a common line denoting the southern phase $\Phi_s(t)$ relative to the guide phase employed. In terms of the theory in section 2, S-format plots the quantities $(\psi_i - \gamma_{is})$, equal to $\Phi_g(t) - \Phi_s(t)$ for southern-dominated oscillations (equation (3d)). These values approach near-constancy if the guide period is close to the southern period. Similarly in N-format, the r component phase data are plotted as measured with 90º being subtracted from the φ component values as before, while 180º is now subtracted from (or equivalently added to) the θ component values, such that for oscillations dominated by the northern system, all these values lie on a common line denoting the northern phase $\Phi_n(t)$ relative to the guide phase employed. N-format thus plots the quantities $(\psi_i - \gamma_{in})$, equal to $\Phi_g(t) - \Phi_n(t)$ for northern-dominated oscillations (equation (3e)), the values approaching near constancy if the guide period is close to the northern period.

[42] If we consider the limiting case of equal amplitudes of the two oscillations, $k = 1$, the results in panel (b) of Figure 2 show that the S-format values raster through ±90º about $\Phi_g(t) - \Phi_s(t)$ (i.e., through half of the full 360º range), while simultaneously, the phase values in N-format raster through ±90º about $\Phi_g(t) - \Phi_n(t)$, thus allowing both southern and northern phases to be determined from fits to the banded phase data in the two formats. If k departs from unity toward smaller (southern dominant) values, the data in S-format become more tightly banded about the southern phase as shown in panel (a) of Figure 2, while the data in N-format become less tightly banded about the northern phase, until the latter banding can no longer be discerned within the uncertainties in the data. Similarly, if k departs from unity toward larger (northern dominant) values, the data in N-format become more tightly banded about the northern phase as shown in panel (c) of Figure 2, while the data in S-format become less tightly banded about the southern phase, until the latter banding can no longer be discerned within the uncertainties.

[43] The limits on the range of k within which the two phases can be discerned by these means can be estimated by noting that when k is small, the phase deviations (in radians) of the combined oscillations about the southern phase are of magnitude $|\delta| \sim k$ (equations (2b) and (2d)), while when k is large, the deviations about the northern phase are of magnitude $|\delta| \sim 1/k$ (equations (2c) and (2e)). Supposing the uncertainties in the phase measurements are $\sim \delta\psi$ (radians), and that the phase deviations in the combined oscillations can only be determined with sufficient accuracy when $|\delta| > f\Delta\psi$ for some $f > \sim 1$, then the range of k for which both phases can be discerned is given by $(f\delta\psi) < k < 1/(f\delta\psi)$. To obtain an estimate, we consider phase measurement uncertainties of $\sim 10º$ as indicated in section 3.2, together, e.g., with $f \approx 1.25$,

giving $f\delta\psi \approx 0.2$ radians. The range of k for which the method will yield both phases is thus roughly a factor of ~ 5 about unity, i.e., $0.2 \leq k \leq 5$. Outside this range, only the southern phase can be determined when k is small and only the northern phase when k is large.

[44] To determine the southern and northern phases when k lies within this range, *Andrews et al.* [2012] calculated piecewise linear fits to the S- and N-format data (using methods appropriate to modulo 360º angular data outlined in section A.2 of Appendix A), employing successive sets of 25 data points typically spanning ~ 200 days. Each fit was taken to define the phase and period of the southern- and northern-system oscillations at the center time of the data set employed. The sequence of such values obtained from data sets shifted one data point at a time, typically separated by ~ 10 days, with linear interpolation between, was then taken to define these quantities over time. While this procedure was successfully applied by *Andrews et al.* [2012] to extended interval E1, it is evidently not appropriate to the later data considered here, where abrupt changes in properties occur on similar ~ 200 day time scales. Here for the later interval, we thus simply employ piecewise linear fits to the individual intervals E2–E4 containing near-steady oscillation properties, as described in section 3.3. Having determined the north and south phases, $\Phi_{n,s}(t)$, the beat phase $\Delta\Phi(t)$ then follows from their difference (equation (2h)). The value of k for any interval is then determined from fitting to the beat phase-dependent phase modulations of the observed combined oscillations, using either the deviations of the ψ_i phase data from the linear fits and equation (3d) or equivalently (3e) as in the study by *Andrews et al.* [2012] or the $\Delta\psi_{r-\theta}$ and $\Delta\psi_{\varphi-\theta} - 90°$ phase difference data and equation (2g). Given both the beat phase and k, the amplitudes of the northern and southern oscillations for each field component can then be estimated from fits to the pass-to-pass amplitude data, using equations (2j) and (2k).

[45] Figure 6 overviews the phase results obtained using these and related methods, to be discussed in detail in sections 4.2. As in Figure 5, vertical dashed lines demarcate intervals E1–E4 having differing oscillation properties, as indicated at the top of the plot. The solid circles in panel (a) show the ψ_i phase data plotted in S-format for the r (red), θ (green), and φ (blue) field components, using a guide phase corresponding to a fixed period of 10.70 h. Two full cycles of phase are plotted on the vertical axis to clearly display the continuity of the data, with each data point being plotted twice. The black crosses and black solid, dotted, and dashed lines show determinations of the southern phase (modulo 360º), while the various purple and green lines similarly show the modeled phases of the observed combined (r, φ) and θ component data, respectively. Panel (b) then shows the same phase data plotted in N-format using a guide phase corresponding to a fixed period of 10.64 h, together with northern phase determinations (black crosses and lines) and phase models for the observed combined data (purple and green lines), in the same figure format as panel (a). The solid circles in panel (c) show the phase difference data $\Delta\psi_{r-\theta}$ (red) and $\Delta\psi_{\varphi-\theta} - 90°$ (blue) as in panel (d) of Figure 5, while the black solid, dotted, and dashed lines show modeled variations. In panel (d), the crosses and solid, dotted, and dashed lines show the oscillation periods corresponding to the gradient of the phase
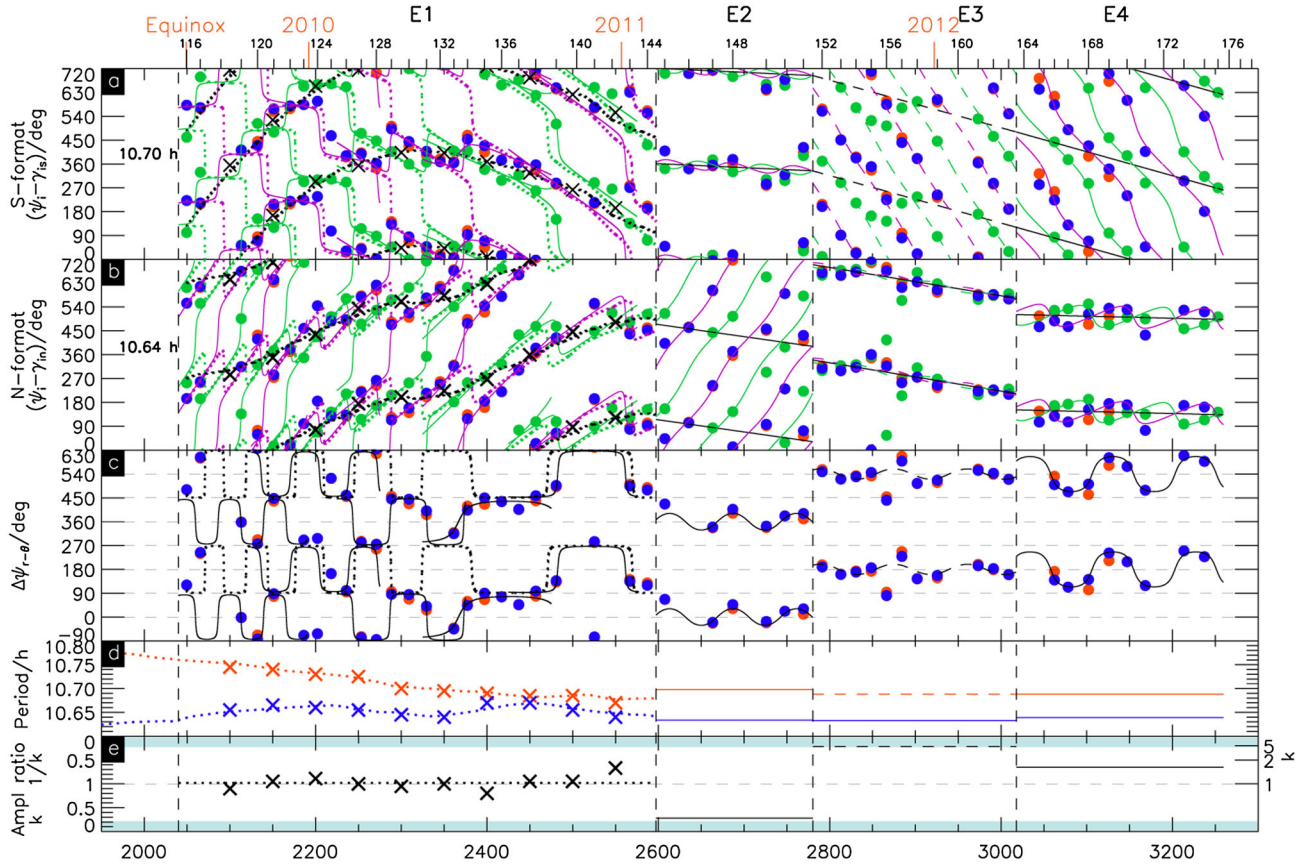
Figure 6. Phase data and derived oscillation parameters plotted versus time over the interval of the study. Periapsis markers and year boundaries are shown at the top of the figure in the same format as Figure 5, together with interval identifiers delimited by the vertical black dashed lines. The panels show (a) phase data ψ_i (solid circles) plotted in S-format (see section 4.1) for the r (red), θ (green), and φ (blue) field components using a guide phase corresponding to a fixed period of 10.70 h, together with model values shown by the black crosses and black, purple, and green lines in various formats as detailed below; (b) the same phase data plotted in N-format using a guide phase corresponding to a fixed period of 10.64 h, together with model values as also indicated below; (c) phase difference data (solid circles) $\Delta\psi_{r-\theta}$ (red) and $\Delta\psi_{\varphi-\theta} - 90°$ (blue) as in Figure 5 together with model values shown by black solid, dotted, and dashed lines; (d) southern (red) and northern (blue) oscillation periods corresponding to the gradients of the modeled phases shown by crosses and solid, dotted, and dashed lines as detailed below; and (e) north/south amplitude ratio k values shown by black crosses and solid, dotted, and dashed lines, where in the lower half of the panel the scale is linear in k from zero to unity, while in the upper half it is linear in $1/k$ between unity and zero (corresponding to k values between unity and infinity as indicated on the right side of the panel). Two full cycles of phase are plotted in panels (a)–(c), with each data point and phase model curve being plotted twice. In panel (e), the two blue bands show the k ranges where the northern properties are inaccessible for small k and the southern properties for large k, while the white band between indicates the range of values ($0.2 < k < 5$) within which we anticipate being able to diagnose both northern and southern oscillation properties using the method of *Andrews et al.* [2012]. In interval E1, the dotted lines in each panel show the model parameters derived by *Andrews et al.* [2012], where in panels (a) and (b), the black dotted lines show the southern and northern phase models, respectively, while the purple and green dotted lines show models for the observed combined phase data for the (r, φ) and θ components, respectively. The crosses and solid lines in interval E1 similarly show the values derived here from 5-parameter fits to 150 day data segments computed every 50 days centered on the times indicated by the crosses, where to avoid multiple overlapping lines only every other fit curve is shown. In E2-E4, the solid lines show results from linear fits to the S- and N-format phase data within those intervals. In E3, the dashed lines indicate values determined using a southern phase that is linearly interpolated between the end of E2 and the beginning of E4 as shown in panel (a).

determinations for the southern (red) and northern (blue) systems. Similarly in panel (e), the black crosses and solid, dotted, and dashed lines show the north/south amplitude ratio k determinations, where below the horizontal short-

dashed line at $k = 1$ the scale is linear in k from zero to unity, while above the horizontal dashed line, it is linear in $1/k$ between unity and zero as marked on the left side of the panel, the latter corresponding to k between unity and
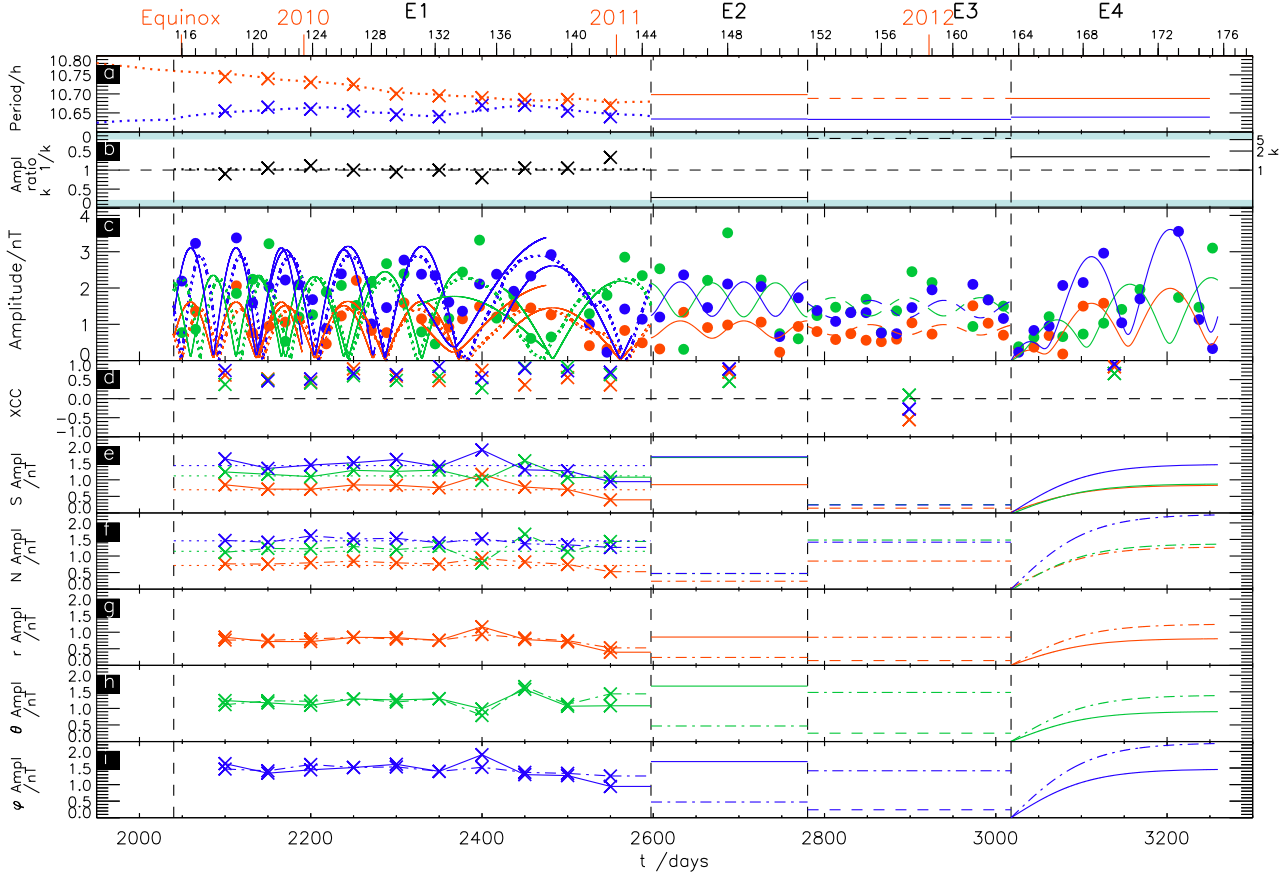
Figure 7. Amplitude data and oscillation parameters plotted versus time over the interval of the study in a similar format to Figure 6. The panels show (a) the oscillation periods as in Figure 6d; (b) the north/south amplitude ratio k as in Figure 6e; (c) amplitude data (solid circles) for the r (red), θ (green), and φ (blue) field components together with model fits shown by similarly colored solid, dotted, and dashed lines as detailed below; (d) similarly color-coded cross-correlation coefficients between the amplitude data and modeled values; (e) separated amplitudes of the southern oscillations for each color-coded field component shown by crosses and solid, dotted, and dashed lines as detailed below; (f) separated amplitudes of the northern oscillations for each color-coded field component similarly shown by crosses and dot-dashed and dotted lines; and (g)-(i) southern (solid and dashed lines) and northern (dot-dashed lines) amplitudes shown separately for the r, θ, and φ field components, respectively, using the same color and line formats as in Figures 7e and 7f. Figures 7e–7i use the same amplitude scale as Figure 7c, though not the same range. As in Figure 6, the dotted lines in interval E1 show the values derived by *Andrews et al.* [2012]. The crosses and solid and dot-dashed lines in E1 show values derived here from five-parameter fits in 150 day data segments computed every 50 days centered on the times indicated by the crosses, where only every other fit is shown in Figure 7c to avoid multiple overlapping lines. The amplitude models in intervals E2-E4 are based on the linear phase models and k values for those intervals shown in Figure 6. In Figures 7e–7i, the solid and dashed lines refer to southern system amplitudes and the dot-dashed lines to northern system amplitudes throughout. In E3, the dashed lines indicate southern values determined using a southern phase linearly interpolated between the end of E2 and the beginning of E4.

infinity, as marked on the right side of the panel. The blue bands at the top and bottom of panel (e) show the ranges of k where the northern properties are inaccessible for $k < 0.2$ and the southern for $k > 5$ (i.e., for $1/k < 0.2$), while the white band between them corresponds to the k range within which we anticipate being able to diagnose both northern and southern phases using the *Andrews et al.* [2012] method.

[46] Corresponding results for the oscillation amplitudes are shown in Figure 7, where again detailed discussion will be given in sections 4.2. For ease of cross-reference, panels (a) and (b) show the oscillation periods and the amplitude ratio k, respectively, in the same format as Figure 6. The solid circles in panel (c) then show the amplitude data for the r (red), θ (green), and φ (blue) field components, together with modeled values shown by the similarly colored solid, dotted, and dashed lines. The crosses in panel (d) then show similarly color-coded cross-correlation coefficients between the amplitude data and the model values in each data segment. The crosses and solid, dotted, and dashed lines in panel (e) show color-coded southern system amplitudes for each field component, while the dot-dashed and dotted lines

in panel (f) similarly show color-coded northern system amplitudes for each field component. In panels (g)-(i), the same amplitude results are shown separately for each field component for both southern (solid and dashed lines) and northern (dot-dashed lines) systems, using identical color and line formats as in panels (e) and (f). We note that panels (e)-(i) all use the same amplitude scale as panel (c) (though not the same range).

4.2. Interval E1

[47] We now discuss the contents of these figures for each of the data intervals identified, beginning with E1, which we note is essentially the interval in common with the analysis presented by *Andrews et al.* [2012]. As defined here, it encompasses the interval from Rev 116 when the spacecraft orbit once more became near-equatorial to Rev 144 after which the oscillation character changed, spanning $t \simeq 2040 - 2597$ days corresponding to August 2009 to February 2011. The top two panels of Figure 6 clearly show the simultaneously and similarly banded nature of the E1 phase data plotted in both S- and N-formats during this interval, indicative of k values near to unity. According to the discussion in section 4.1, these bands thus reveal the phase variations of the southern and northern oscillations, respectively, relative to the chosen guide phases. Slowly rising or falling values indicate oscillation periods that are slightly longer or shorter than the guide periods, respectively. The results derived by *Andrews et al.* [2012] are shown by the dotted lines in each panel, where the black dotted lines in panels (a) and (b) show the southern and northern phases, respectively, while the purple and green dotted lines show the model phases for the observed combined oscillations of the (r, φ) and θ field components, respectively, using a best-fit value of $k = 1.02$, shown by the horizontal dotted line in panel (e). These models clearly provide a good account of the phase data. The corresponding southern and northern periods are shown by the red and blue dotted lines, respectively, in panel (d), which converge to an almost common value ~10.68 h near $t \approx 2450$ days (mid-September 2010), just over one year after equinox, before modestly diverging again in the same sense as before.

[48] Here we have also explored an alternative fitting strategy to these data, which also yields improved time resolution on the amplitude ratio k, a topic of particular interest for reasons introduced in section 3. Specifically, we have used the theory in section 2 to fit directly to the (r, φ) and θ phase values in individual time segments. The model is thus a function of five parameters, namely, the slope and intercept of the northern and southern phase functions $\Phi_{n,s}$ (t), assumed to vary linearly with time during each data segment (i.e., fixed periods), and the amplitude ratio k. The method is simply to find the set of five parameters that gives the minimum variance between the model and the data (equation (A3)) within a five-dimensional parameter "cube" spanning appropriate ranges. The steps employed were 7.2º for the phase constants, 0.005 h for the periods, and 0.05 for k when $k \leq 1$ and similarly for $1/k$ when $k \geq 1$. In addition, to treat more equally the phases of the oscillations in the north-south and equatorial field components, for which there is generally one measurement of the former (θ component) and two of the latter (both r and φ) from each

pass, we have also averaged the ψ_r and $\psi_\varphi - 90°$ data together for a given pass (equation (A1)) when both are available, thus forming averaged "purple" data from the red and blue data shown in Figure 6. If either ψ_r or $\psi_\varphi - 90°$ is not available, the remaining value is used unmodified. The model is then fitted to the green and "purple" data in each time segment. The chosen overlapping segments are centered every 50 days throughout E1, comprising 10 evaluations overall, each encompassing data within ± 75 days on either side (similar to the $\pm$~100 day sequences employed by *Andrews et al.* [2012]). This choice ensures that each data segment contains at least one half-beat period, a requirement if the difference between the southern and northern periods is to be accurately determined (see panel (b) of Figure 2). However, fits using data windows of ± 50 and ± 100 days about the same times show that the results are not sensitively dependent on this choice.

[49] The results show that although there are often a number of local variance minima within the parameter "cube," one clear global minimum is generally evident, with typical minimum variance values (see equation A3) of ~0.05 to ~0.1, implying modest deviations between the phase data and model of typically ~20º to ~25º. The piecewise fits are shown by the solid green and purple lines in panels (a) and (b) of Figure 6 and by the solid black lines in panel (c), though these are shown only for every other data segment to avoid confusion of multiple overlapping lines. The southern and northern phase values at the center of each data segment are shown by the black crosses in panels (a) and (b), respectively, and can be seen to agree closely with those derived by *Andrews et al.* [2012] (black dotted lines). Similarly, the southern and northern periods shown by the red and blue crosses in panel (d), respectively, are also found to agree closely with the values (red and blue dotted lines) of *Andrews et al.* [2012]. The amplitude ratios k shown by the crosses in panel (e) show values consistently close to unity, with an average over the interval of 1.03, compared with the overall value of 1.02 determined by *Andrews et al.* [2012] (horizontal black dotted line). In the initial part of the interval to ~2350 days, the individual values lie consistently close to unity, between ~0.9 and ~1.1. After this, however, a departure to somewhat smaller values of k~0.8 occurs near 2400 days and to somewhat larger values of k~1.3 at 2550 days, thus quantifying the variations noted previously in the phase difference data in section 3.3.

[50] The colored lines in panel (c) of Figure 7 similarly show model values fitted to the E1 amplitude data (similarly colored solid circles) using the beat phase and k values obtained from the phase analysis just described. The dotted lines again show the values determined by *Andrews et al.* [2012], while the solid lines show the values derived here from the five-parameter phase fits, with results again being shown for every other data segment. The model values are strongly modulated at the beat period due to the $k \approx 1$ conditions prevailing and can be seen generally to provide a reasonable description of the data. The cross-correlation coefficients shown in panel (d) are generally positive lying between +0.3 and +0.9, with averaged values of +0.54 for r, +0.46 for θ, and +0.66 for φ. The results in panels (e)–(i) show that during the initial part of E1 to $t \approx 2350$ days, the northern and southern system amplitudes are near-constant in time and near-equal in value, in line with the $k \approx 1$ conditions just

Table 1. Oscillation Periods, Amplitude Ratios, and Amplitudes for Intervals E1-E4

Interval	E1 Revs 116–144	E2 Revs 145–151	E3 Revs 152–163	E4 Revs 164–175
North period/h	10.656[a] 10.640–10.670	10.634 ± 0.005	10.633 ± 0.002	10.639[f] ± 0.002
South period/h	10.707[a] 10.670–10.745	10.698 ± 0.003	10.688[c]	10.688[f] ± 0.004
North/South amplitude ratio k	1.03[a] 0.80–1.33	0.32 ± 0.07[b]	6[d] ± 2[b]	1.6[f] ± 0.3[b]
North r-component amplitude/nT	0.79[a] 0.53–0.94	0.27	0.85	1.22[g]
North θ-component amplitude/nT	1.25[a] 0.89–1.64	0.53	1.48	1.39[g]
North φ-component amplitude/nT	1.44[a] 1.26–1.61	0.54	1.42	2.23[g]
South r-component amplitude/nT	0.80[a] 0.40–1.17	0.85	0.14 [e]	0.78[g]
South θ-component amplitude/nT	1.22[a] 1.07–1.56	1.66	0.25 [e]	0.89[g]
South φ-component amplitude/nT	1.44[a] 0.95–1.90	1.68	0.24 [e]	1.43[g]

[a]Averaged value and range over the ten 150-day fits spanning interval E1.
[b]Value obtained from the k range about the best fit required to produce a 10% increase in the square root of the variance between the phase data and the model, see section 4.3.
[c]Value determined by linear interpolation of the southern phase between the end of interval E2 and the beginning of interval E4.
[d]Determined from the fit to the $\Delta\psi_{r-\theta}$ phase difference data excluding Revs 156 and 157, using the interpolated southern phase.
[e]Determined from the northern amplitudes using the E3 k value derived using the interpolated southern phase.
[f]Determined from phase data for Revs 166-175.
[g]Limiting amplitudes of hyperbolic tangent fit to amplitude data with $\tau = 86$ days, see section 4.5.

discussed. The amplitudes of both systems are ~0.8 nT for r, ~1.2 nT for θ, and ~1.5 nT for φ, in good agreement with the *Andrews et al.* [2012] values shown by the dotted lines in panels (e) and (f). The reduced value of $k \simeq 0.8$ near ~2400 days is then related principally to an increase in the southern amplitude for the r and φ components and to a decrease in the northern amplitude for the θ component. Opposite variations then give rise to the increased value of $k \approx 1.3$ near ~2550 days.

[51] The oscillation parameters determined here from the five-parameter fits are recorded in Table 1 and Table B1 in Appendix B. Specifically, in Table 1, we give the averaged values and ranges of the periods, the amplitude ratio k, and the amplitudes of each field component for both northern and southern systems. In Table B1, we record the parameters of the phase functions (see Appendix B) and k values for each individual 150 day fit.

4.3. Interval E2

[52] We now turn to the previously unmodeled data in interval E2 encompassing Revs 145–151, $t \simeq 2597 - 2780$ days corresponding to February to August 2011. Examination of the S- and N-format phases in panels (a) and (b) of Figure 6 shows that the character of these data is considerably and rather abruptly altered compared with E1, with the S-format data being more tightly banded than before, while the N-format data are much less tightly banded, particularly later in the interval. These data thus show that the southern oscillations unexpectedly resume dominance during this interval ~1.5-2 years after equinox as inferred in section 3.3, with the $\Delta\psi_{r-\theta}$ and $\Delta\psi_{\varphi-\theta} - 90°$ phase difference data in panel (c) varying modestly about 0º (modulo 360º). Panel (a) also shows that a distinct change in the slope of the southern phase values took place between the two intervals, indicative of an increase in period close to the 10.70 h guide period, combined with a jump in the phase itself. We note that abrupt behavior of this

nature has not been documented previously in related studies of magnetic oscillation data.

[53] The black line in panel (a) of Figure 6 shows an individual linear fit to the E2 S-format data taken as a whole (section A.2), equivalent to the method of *Andrews et al.* [2012], though we have again averaged the ψ_r and $\psi_\varphi - 90°$ data together (when both are available) before performing the fit for reasons given in section 4.2 above. This fit yields a well-defined southern system period of 10.698 h, close to the guide period employed, shown by the red line in panel (d). The uncertainty in this value is estimated to be $\pm \sim 0.003$ h (i.e., $\pm \sim 10$ s), based on the estimated uncertainty in the slope of the fit. This period compares with values of 10.685 and 10.670 h determined from the last two data segments in E1 (Table B1), the latter indicating a modest but clear ~0.25% (~100 s) increase in the southern period in E2. In addition, the fitted phases decreased by ~100º across the interval boundary, implying a significant jump in phase of the southern oscillations. In effect, the azimuth of the rotating quasi-uniform equatorial field (and related north-south field) advanced through this angle during the ~20 day interval in February 2011 between the periapsis passes of Revs 144 and 145. Although this fit represents the E2 data reasonably well, particularly for Revs 145–148 in the early part of the interval, the later data from Revs 149–151 show greater scatter about this line. However, this is not produced by beats between the northern and southern oscillations, where the (r, φ) and θ phases deviate in opposite directions but rather has the form of "common jitter" in which all the phases from a given pass vary together in a given sense. Such additional pass-to-pass variations have previously been inferred by *Provan et al.* [2011] from data obtained during the initial near-equatorial Cassini orbit interval in 2004–2006 (interval A in the nomenclature of *Andrews et al.* [2012]) and were suggested as possibly associated with solar wind speed-related SKR phase variations reported by *Zarka et al.* [2007]. The RMS

Table B1. Northern and Southern System Oscillation Phase Models for Intervals E1–E4

Interval	Start-end time days[a]	Amplitude ratio k	Φ_{0n}/deg	τ_n/hr	Φ_{0s}/deg	τ_s/hr
E1–1	2025–2175	0.90	316.8	10.655	266.4	10.745
E1–2	2075–2225	1.05	144.0	10.665	180.0	10.740
E1–3	2125–2275	1.11	36.0	10.660	352.8	10.730
E1–4	2175–2325	1.00	237.6	10.655	280.8	10.725
E1–5	2225–2375	0.95	316.8	10.645	316.8	10.700
E1–6	2275–2425	1.00	136.8	10.640	151.2	10.695
E1–7	2325–2475	0.80	172.8	10.670	338.4	10.690
E1–8	2375–2525	1.05	194.4	10.670	136.8	10.685
E1–9	2425–2575	1.05	252.0	10.655	144.0	10.685
E1–10	2475–2625	1.33	237.6	10.640	136.8	10.670
E2	2597–2780	0.32	134.8	10.634	326.1	10.698
E3	2780–3018	6[b]	334.0	10.633	52.1[c]	10.688[c]
E4	3018–3259	1.6	338.2	10.639	23.2	10.688

[a]Note $t = 0$ corresponds to 00 UT on 1 January 2004.
[b]Determined from the fit to the $\Delta\psi_{r-\theta}$ phase difference data excluding Revs 156 and 157, using the interpolated southern phase.
[c]Value determined by linear interpolation of the southern phase between the end of E2 and the beginning of E4.

value of the "common jitter" was inferred to be ~10° in those data, while the values indicated here on Revs 149–151 are up to ~50°. Due to these variations, the five-parameter fit method introduced for E1 cannot be appropriately applied to these data, since it assumes that the dominant variations are due to beats between the northern and southern systems, which is clearly not true overall in this case.

[54] The fit to the N-format data in panel (b) of Figure 6 is also seen to be well constrained by the data banding in the first half of E2, in this case suggesting an insignificant ~20° jump in northern oscillation phase across the boundary. However, it is clearly less well constrained in the second half of the interval, indicating greater uncertainty in the phase slope and hence period. The period obtained from the fit, 10.634 h ($\pm$~0.005 h) shown by the blue line in panel (d), is nevertheless closely similar to but slightly smaller than the values of 10.655 and 10.640 h obtained from the last two data segments in E1, thus continuing the slow fall in northern period from peak values of ~10.67 h at the time of near-coalescence. The gap between southern and northern periods thus also continued to widen, with the southern period remaining longer than the northern as found at the end of E1 both here and by *Andrews et al.* [2012]. The difference in periods was 0.030 $\pm$ 0.004 h (~2 min) at the end of E1 and 0.064 $\pm$ 0.006 h (~4 min) in E2, thus approximately doubling in value. The corresponding beat periods were ~160 $\pm$ 20 days at the end of E1 and ~75 $\pm$ 7 days in E2.

[55] Given the model fits for the northern and southern oscillation phases, and hence the beat phase, the north/south amplitude ratio k for the interval can be determined by fitting the theoretical model expressions in section 2 to the observed beat-modulated phases. *Andrews et al.* [2012] fitted equations (2b)–(2e) to the deviations of the $\psi_i - \gamma_{in,s}$ data from the linear fits, but this procedure is somewhat compromised in the present case by the presence of the large "common jitter" noted above. Instead, we have therefore fitted equation (2g) to the $\Delta\psi_{r-\theta}$ and $\Delta\psi_{\varphi-\theta} - 90°$ phase difference data, from which "common jitter" is perforce eliminated, giving a possibly reduced but cleaner data set to which to fit. This method has then been applied uniformly to the three data intervals E2–E4. For interval E2, the best fit to these data, obtained by searching for the k value that gives the minimum variance V (equation (A3)) between the data and

the model using k steps of 0.01, yields a value of $k \simeq 0.32$ as indicated in Table 1. Formal uncertainties are again difficult to assign, but a useful measure may be found by considering the change in k about the minimum required to produce a significant 10% increase in $\sqrt{2V}$, the latter being approximately the RMS deviation (in radians) between the data and the model for small V (section A.2). This range of k is found to be ~0.07, also given in Table 1. The above best-fit value $k \simeq 0.32$ is seen to yield a good fit to the E2 phase difference data, as shown by the black solid line in panel (c) of Figure 6, and also provides a tolerable fit to the phase deviations relative to the linear phase models in panels (a) and (b), shown by the purple and green solid lines. The value is comparable with but somewhat smaller even than the value $k \sim 0.4$ determined for southern summer conditions by *Provan et al.* [2011] and *Andrews et al.* [2012] and lies only modestly above the limiting range for which northern parameters cannot be derived from the phase data ($k < 0.2$), shown by the lower blue band in panel (e) of Figure 6.

[56] Using these beat phase and k values, we can then fit to the E2 amplitude data in panel (c) of Figure 7 to determine the northern and southern system amplitudes during the interval. With the occasional exception, the model fits shown by the solid lines are seen to agree with the rise and fall of the observed values caused by the beat effect, with consistently positive cross-correlation coefficients of +0.70 for r, +0.46 for θ, and +0.78 for φ. Examination of the amplitudes themselves in panels (e)–(i) of Figure 7 shows that the resumption of southern-system dominance in interval E2, compared with near-equal amplitudes in interval E1, is due to both an increase in the southern amplitude by a modest factor of ~1.3 and a major decrease in the northern amplitude by a factor of ~2.5. The former increase results in southern system amplitudes that are almost identical to those occurring during southern summer, 0.85 nT for r, 1.66 nT for θ, and 1.68 nT for φ (Table 1), compared with 0.86 nT for r, 1.65 nT for θ, and 1.71 nT for φ obtained by *Andrews et al.* [2012] in intervals A/C in 2004–2007. The latter decrease then results in northern system amplitudes that are somewhat lower even than those occurring during southern summer, 0.27 nT for r, 0.53 nT for θ, and 0.54 nT for φ (Table 1), compared with 0.33 nT for r, 0.63 nT for θ, and 0.65 nT for φ in intervals A/C.

4.4. Interval E3

[57] Turning now to interval E3 encompassing Revs 152–163, $t \simeq 2780 - 3018$ days corresponding to August 2011 to March 2012, it can be seen in panels (a) and (b) of Figure 6 that the phase data have again undergone an abrupt and marked change in properties. The N-format phase data are now tightly banded while the S-format data are essentially unbanded, indicative of strong northern oscillation dominance for the first time in these data. Correspondingly, the $\Delta\psi_{r-\theta}$ and $\Delta\psi_{\varphi-\theta} - 90°$ phase difference data in panel (c) generally vary modestly about 180°, with the exception of Revs 156 and 157 near ~2875 days (November 2011) where the deviations are significantly larger as mentioned in section 3.3. It is notable that the transition from southern dominance in E2 to northern dominance in E3 occurred abruptly between the periapses of Revs 151 and 152, separated by only 22 days.

[58] The black line in panel (b) of Figure 6 shows a linear fit to the N-format data, yielding a northern system period of 10.633 h ($\pm \sim 0.002$ h) shown by the blue line in panel (d). This value is essentially the same as the 10.634 h ($\pm \sim 0.005$ h) northern period derived for E2, such that there is no evidence of a change in northern system period between the two intervals. There is, however, a jump in fitted phase of ~50° across the boundary of the two intervals, but in view of the weakly banded nature of the N-format data toward the end of E2, this is not considered significant. Application of the same technique to the S-format data, however, yielded no significant minima in the variance over the expected range of periods, either for the whole of E3 or for a number of 150 day subintervals that were investigated. Nevertheless, the phase difference data in panel (c) show weak deviations about 180°, which we have attempted to model using a three-parameter fit as outlined in section 4.3. Again, the results were not conclusive, the variance displaying a number of similar weak minima in the expected range.

[59] The conclusion therefore is that the southern amplitude during E3 was sufficiently low compared with the northern that the southern oscillation parameters cannot reliably be determined, implying $k > \sim 5$ according to the discussion in section 4.1. However, it is noted that when the southern phase determined from E4 data (section 4.5) is projected back in time at constant period, the value is found to lie very close to that of the well-determined southern phase at the end of E2. We have therefore investigated whether a southern phase linearly interpolated between the end of E2 and the beginning of E4, shown by the black dashed line in panel (a) of Figure 6, provides a fit to the phase difference values. We note that the slope of this line corresponds to a period of 10.688 h (very close to that in E4), implying a difference in periods in E3 of 0.055 h with a corresponding beat period of ~86 days. Excluding the large values for Revs 156 and 157, the best fit to the data in panel (c) is found for $k \simeq 1/0.17 \approx 6$, thus lying just beyond the $k > \sim 5$ limit shown by the upper blue band in panel (e). The uncertainty in this k value, determined as outlined in section 4.3, is $\pm \sim 2$ (Table 1). The best fit is shown by the dashed line in panel (c), where it can be seen that (with the exception of Revs 156 and 157) this model provides a consistently reasonable description of the magnitude and sense of the phase difference data, thus lending modest credence to the interpolated southern phase.

[60] The best fits to the E3 amplitude data in panel (c) of Figure 7 using the above parameters, however, are found to show little correspondence with the variations of these data, with cross-correlation coefficients that are either small or negative, -0.55 for r, +0.09 for θ, and -0.27 for φ. Scattered results were also obtained for selected subsets of the data. It thus seems clear that other sources of amplitude variability swamp the expectedly modest beat-phase amplitude effects in E3, it being noted in particular that values in the second half of the interval tend to be larger than in the first, though returning to initial values toward the end. In these circumstances, the best-fit values in effect determine the amplitudes of the dominant northern oscillations, with the southern amplitudes being given simply through the amplitude ratio k. The northern amplitudes are thus estimated as 0.85 nT for r, 1.48 nT for θ, and 1.42 nT for φ, as shown in panel (f) of Figure 7 (Table 1), while the southern amplitudes are 0.14 nT for r, 0.25 nT for θ, and 0.24 nT for φ, shown by the dashed lines in panel (e). These results thus indicate that the abrupt change between E2 and E3 was due to an increase in the northern amplitude by a factor of ~3.0 back to values comparable to E1, combined with a simultaneous decrease in the previously near-constant southern amplitude by a factor of ~6 to values of a few tenths of a nT.

4.5. Interval E4

[61] A further abrupt change then occurred in interval E4, encompassing Revs 164 to the end of the data considered here at Rev 175, $t \simeq 3018 - 3259$ days corresponding to April to November 2012. As illustrated in plot (e) of Figure 4, this change is presaged in Rev 164 where for the first time in these data, the core region amplitudes in all three field components were sufficiently low (~0.2-0.4 nT) that no phases could reliably be determined. Over the following Revs, the amplitudes then recovered to more normal values as seen in panel (c) of Figure 7, such that phases can once more be determined for both (r, φ) and θ components for Rev 166 and later (except for the r components for Revs 170–175 due to ring current effects associated with the increasing tilt of the orbit plane (section 3.3)). We recall that no results are available for Rev 172 due to an extended magnetic field data gap. Figure 6 shows that the N-format phase data in panel (b) continue to be tightly banded, though somewhat less so than for E3, while the S-format data in panel (a) now exhibit evident but weaker banding in the later interval where both (r, φ) and θ component data are available. These properties indicate that the northern oscillations remain dominant in E4, though less so than during E3, such that the phase difference values in panel (c) continue to oscillate about 180° but with a markedly larger amplitude.

[62] The solid black lines in panels (a) and (b) of Figure 6 show linear fits to the Rev 166–175 data in both cases, yielding a northern period of 10.639 h ($\pm \sim 0.002$ h) from the N-format data and a southern period of 10.688 h ($\pm \sim 0.004$ h) from the S-format data, shown by the blue and red lines, respectively, in panel (d). The northern period is slightly longer than those determined for both E2 and E3, with the change in the slope of the phase being clear between E3 and E4 in the tightly banded N-format data. Overall, however, these results indicate an approximately constant northern period ~10.635 h over E2-E4, significantly shorter than the maximum value of 10.670 h ($\pm$0.0025 h) that occurred in the interval of near-coalesced periods in E1. The fitted northern phases also exhibit a jump of ~60° across the boundary between E3 and E4. The E4 southern

period of 10.688 h ($\pm \sim 0.004$ h) is very nearly the same as the interpolated value for E3 and also similar to the value in interval E1 when the periods near-coalesced of 10.685 h (± 0.0025 h) within the uncertainty estimates, though being somewhat shorter than the value in E2 of 10.698 h (± 0.003 h), outside of the uncertainty estimates. The difference period in E4 of 0.049 ± 0.004 h is thus slightly reduced compared with E2 and that inferred for E3, with a corresponding beat period of ~95 $\pm$ 8 days.

[63] Using a fit to the phase difference data in panel (c) of Figure 6, as for the other intervals, the best fit k value for interval E4 is found to be $k \simeq 1/0.64 \approx 1.6$, with an uncertainty determined as in section 4.3 of $\pm \sim 0.3$. The dominance of the northern oscillations is thus significantly less in E4 than in E3, for which we estimated $k \approx 6$. It can be seen that the model provides a good fit to the phase difference data in panel (c) of Figure 6 and also gives a good account of the modulations of the individual (r, φ) and θ phase data about the linear fits in panels (a) and (b).

[64] It is clear, however, that a fit to the amplitude data in panel (c) of Figure 7 using constant amplitudes for the northern and southern systems is inappropriate in view of the evident increase in amplitudes from small values over the interval. Here we have therefore used a simple hyperbolic tangent variation in equations (2j) and (2k) to represent the rise from small to near-constant values, given for field component i by

$$B_{0in}(t) = kB_{0is}(t) = B_{0in} \tanh\left(\frac{(t - t_o)}{\tau}\right), \qquad (4)$$

where t_o is taken to be the start of interval E4 ($t_o \simeq 3018$ days), τ is the amplitude growth time, and B_{0in} are the limiting northern amplitudes at large time for component i, the limiting southern amplitudes being B_{0in}/k. The fit giving the minimum RMS deviation between data and model is found to have $\tau \approx 85$ days, approximately one third of the length of the E4 interval (~240 days). However, models with τ between ~70 and ~110 days are found to fit almost as well. The best-fit limiting amplitudes for the northern system are 1.22 nT for r, 1.39 nT for θ, and 2.23 nT for φ, with corresponding limiting amplitudes for the southern system of 0.78 nT for r, 0.89 nT for θ, and 1.43 nT for φ. These models provide reasonably good fits to the amplitude data in panel (c), particularly for the φ component, with cross-correlation coefficients of +0.84 for r, +0.65 for θ, and +0.91 for φ, as shown in panel (d). It may be noted from Figure 7 and Table 1 that these limiting southern amplitudes are once more comparable to those in E1, though somewhat less than those in E2, while the limiting northern amplitudes are larger than those in E1 (factor ~1.4) and comparable with or larger than those in E3.

5. Summary and Discussion

[65] We have examined the properties of the "planetary period" magnetic field oscillations in Saturn's magnetosphere observed on 56 near-equatorial Cassini periapsis passes through the core region (dipole $L \leq 12$) that occurred between the second and third high-latitude mission phases from August 2009 to November 2012. These passes, on Revs 116–175, had periapsides at ~3-6 R_S in the dawn sector, providing core data

every ~20 days from which the amplitude and phase can be determined for each field component. These data span the first ~3.3 years of the northern spring interval between equinox in August 2009 and northern summer solstice in May 2017.

[66] Previous studies by *Provan et al.* [2011] and *Andrews et al.* [2010b, 2012] demonstrated that the core region oscillations consist of the superposition of two systems with differing polarization characteristics, periods, and amplitudes, which are associated with the northern and southern polar regions. During the initial Cassini southern summer interval, 2004–2007, the southern system was dominant with a north/south amplitude ratio $k \approx 0.4$ and with the southern period ~10.8 h being longer than the northern ~10.6 h. However, *Andrews et al.* [2012] showed that these periods began to converge in late 2008 and reached a near-common value of ~10.68 h in September 2010, just over one year after equinox, reflecting similar behavior in the SKR periods [*Gurnett et al.*, 2010b; *Lamy*, 2011]. In the subsequent ~6 months to early 2011, the two periods then slowly diverged again in the same sense as before. *Andrews et al.* [2012] also showed that the two systems had reached near-equal amplitudes $k \approx 1$ in the postequinox interval, due to a factor ~0.75 reduction in the southern system combined with a factor of ~2 increase in the northern system.

[67] Here we have further investigated the postequinox core region oscillations during the initial ~18 month interval studied by *Andrews et al.* [2012] (interval E1), newly using a direct five-parameter fit to analyze the beat-modulated phase data. This analysis produced results for the phase and period that closely confirm those previously derived, as just outlined, while yielding greater temporal resolution on the northern and southern amplitudes. These are found to be near-constant and near-equal in the two systems (to within ~10%) in the ~10-month interval from equinox to mid-2010, while modest deviations from near-equality then occur during the following ~8-month interval to early 2011 spanning the convergence of the periods, to southern dominant ratios $k \approx 0.8$ prior to the convergence, and to northern dominant ratios $k \approx 1.3$ after the convergence. Amplitude data for the φ component, representing the best defined data set, suggest that the variations were due mainly to changes in the southern system, relative to near-constant amplitudes in the northern system.

[68] These findings provide the first indication of variability in the postequinox oscillation amplitudes on several-month time scales. In the following ~22 month interval newly analyzed here, the oscillations are found to exhibit major abrupt changes in properties on such time scales, quite unlike the steady behavior observed previously during postsolstice southern summer conditions. The changes principally involve abrupt variations in the amplitudes of the two systems, together on occasion with small but clear changes in the period and/or phase. The changes themselves occurred between one periapsis pass and the next, thus on time scales of ~20 days or less. Three such changes have been documented here, occurring in February 2011, August 2011, and April 2012, with lesser changes being noted in November 2011.

[69] At the first of these transitions in February 2011, the northern amplitude decreased by a factor of ~2.5 to values lower even than during southern summer, while the southern amplitude increased modestly by a factor of ~1.3 back to southern summer values. Thus, strongly southern-dominant

conditions with $k \approx 0.32$ were unexpectedly resumed ~1.5 years after equinox, persisting for the following ~6 month interval (interval E2). The linear-fit method of *Andrews et al.* [2012] yields a southern period in E2 of 10.70 h (see Table 1 for more precise values and uncertainty estimates), representing a clear but modest increase relative to the postcoalescence period at the end of E1 of 10.67 h, while the northern period was found to be approximately constant within the uncertainties, being 10.63 h in E2 compared with 10.640 h at the end of E1. In addition, a ~100º jump in the fitted southern phase occurred across the transition, together with a smaller jump in fitted northern phase of ~20º, the latter not being considered significant within the uncertainties.

[70] At the second transition in August 2011, the northern amplitude increased by a factor ~3 back to values similar to E1, while the previously near-constant southern amplitude simultaneously decreased by a factor of ~6 to a few tenths of a nT, such that with $k \approx 6$, the presence of the southern system could hardly be discerned in the phase data. Strongly northern-dominant oscillations were thus first established ~2 years after equinox in an abrupt transition that took place between two Cassini periapsis passes separated by ~20 days. These conditions were maintained for the following ~8 months to April 2012 (interval E3). However, the phase data indicate a brief re-emergence of comparably strong southern oscillations during two Revs in November 2011, indicating the occurrence of unresolved shorter-lived transitions around this time. The northern period in E3 was found to be 10.63 h, the same as in E2 within the uncertainties, remaining modestly shorter than at the end of E1. Though the southern phase could not be determined from the E3 data, linear interpolation between E2 and E4, corresponding to a period of 10.69 h, was found to provide reasonable agreement with the phase modulation data (excepting the November 2011 data) with $k \approx 6$ as just indicated.

[71] The final transition documented here took place in April 2012, with effects that persisted for at least ~8 months to the end of the data set examined here in November 2012 (interval E4). The dominant northern oscillations present during E3 were suppressed from one Rev to the next to values below a few tenths of a nT, such that for one Rev, no clear oscillations were present in the core region in any field component for the first time in these data. Oscillations re-emerged with increasing amplitude over the next several Revs, reaching usual values in the second half of the interval, implying a recovery time scale of ~85 days (i.e., 3 months). The emergent oscillations were again dominated by the northern system but by a lesser factor of $k \approx 1.6$, with limiting northern amplitudes comparable with or larger than in E3, and southern amplitudes comparable with E1. The southern and northern periods were found to be 10.69 h and 10.64 h, respectively, such that the southern period was slightly longer than at the end of E1 but slightly shorter than during E2 (and almost the same as the interpolated value for E3), while the northern period was close to the value at the end of E1 and slightly (but clearly) longer than in E2 and E3. In addition, a jump in the fitted northern phases of ~60º occurred across the E3–E4 boundary.

[72] Although the above discussion of oscillation periods emphasizes the variations that occur from interval to interval in this study, it should be stressed that these are remarkably small over the 22-month postcoalescence interval newly analyzed here, despite the large ~6–8 monthly abrupt changes in amplitude occurring in this interval. Over the interval from February 2011 to November 2012, the oscillations varied in character from being near-equal in amplitude to southern dominant and then to northern dominant, while the northern period varied only over the range from 10.63 to 10.64 h and the southern period from 10.69 to 10.70 h. No systematic widening of the gap between the periods was observed over this interval; indeed, the gap was found to narrow slightly from 0.06 h in E2 to 0.05 h in E4, though both being larger than the value of 0.03 h at the end of E1. Thus although we have documented some clear but small changes in period (and phase) that take place across the abrupt transitions in amplitude, the overall picture is one of stability of the periods. This is perhaps surprising, given that the gap in periods more than three years after equinox and less than six years before the next northern solstice remains less than a quarter of the peak value of ~0.22 h observed in the postsolstice southern summer interval [*Andrews et al.*, 2012].

[73] We finally comment briefly on the relation between these findings and prior physical discussions cited in section 1. Clearly physical models that invoke some essentially equatorial process, related for example to flux tube interchange motions driven by mass loading [*Goldreich and Farmer*, 2007] or ring current asymmetries [*Khurana et al.*, 2009; *Brandt et al.*, 2010], can at most represent only part of the picture, since they miss the fundamental feature of two oscillatory systems associated with the north and south polar regions. Some additional coupling between polar and equatorial regions is then required to generate the two separate systems, with their variable amplitudes and periods, that are the essential phenomena addressed here.

[74] The latter aspect is more natural in models that invoke potentially separate rotating neutral wind systems in the two polar regions as the primary driving mechanism [*Smith*, 2010; *Jia et al.*, 2012]. However, the abrupt simultaneous changes in the amplitudes of the two systems found here pose a significant question concerning how polar wind systems in the two hemispheres could communicate, e.g., to switch off one system and switch on the other on a time scale of ~20 days or less, while evidently being able to co-exist at other times in near-steady conditions over intervals of at least ~6–8 months. One possibility suggested by *Fischer et al.* [2012] is that some of the variations at least could be related to giant thunderstorm activity in the lower atmosphere, it being noted that variations in the southern SKR modulation period that correspond roughly to our interval E2 relate to the growth and decay of a "Great White Spot" at northern tropical latitudes, that rotates with a period ~10.69 h similar to the southern system at that time. However, the temporal correspondence is not exact, with the main tropospheric storm occurring between December 2010 and June 2011, while our interval E2 defined by sequential abrupt (~20 day) changes in field oscillation properties spans February to August 2011. In addition, it remains unclear how a storm at northern tropical latitudes could enhance the amplitude and increase the period of the southern oscillations (though the latter only by 0.25% relative to the end of E1), while at the same time suppressing the northern oscillations but leaving their period unchanged (to within ~0.05%).

[75] Another possibility is that the abrupt changes could be externally triggered by the solar wind, e.g., by strong compressions whose effect might depend on the timing relative to the phasing of the oscillations. It is notable that

the onset of the abrupt behavior in early 2011 coincided with the emergence of the Sun from its recent deep extended minimum in activity cycle, with the appearance of significant flare and CME activity and larger sunspot numbers than any to have occurred since the start of the in-orbit Cassini mission (e.g., http://secchi.nrl.navy.mil/cactus/). Further investigation of correlated behavior is thus warranted, both with regard to the atmospheric disturbances and solar wind variations, together with further observations of the oscillation properties.

Appendix A: Directional Statistics

[76] In this appendix, we provide definitions and formulae appropriate to the analysis of modulo 360º phase data that are employed in our study. These are based on the "directional statistics" approach of *Mardia and Jupp* [2000], as employed previously by *Andrews et al.* [2011, 2012] and *Provan et al.* [2012].

A.1. Mean Value and Standard Deviation

[77] The mean value and standard deviation of a set K of angles θ_k defined to modulo 360º are given by the complex sum

$$\frac{1}{K}\sum_{k=1}^{K} e^{j\theta_k} = \bar{R}e^{j\bar{\theta}}, \tag{A1}$$

where $\bar{\theta}$ is the "directional mean" of the values, and $\bar{R}$ is the "mean resultant length" lying in the range $0 \leq \bar{R} \leq 1$. The "circular standard deviation" σ of the values is then given (in radians) by

$$\sigma = \sqrt{-2\ln\bar{R}}. \tag{A2}$$

A.2. Linear Fits to Phase Data

[78] Here we address the issue of obtaining the best linear fit $\psi = \alpha t + \beta$ to a set of K phase data points ψ_k at t_k, taking account of the modulo 360º nature of the data. A suitable measure of the variance V_{θ_0} of a set of K angles θ_k about some angle θ_0 is given by

$$V_{\theta_0} = \frac{1}{K}\sum_{k=1}^{K}(1 - \cos(\theta_k - \theta_0)), \tag{A3}$$

which we note is equal to half the mean square deviation of the angles (in radians) from θ_0 in the case of small deviations and goes to a value of unity when for every θ_k, there is a corresponding value $\theta_k + 180°$ in the data set. We then wish to find the values of α and β that minimize the variance about zero of $(\psi_k - (\alpha t_k + \beta))$, in other words, the values that minimize

$$V_0 = \frac{1}{K}\sum_{k=1}^{K}(1 - \cos((\psi_k - \alpha t_k) - \beta)) \tag{A4}$$

$$= 1 - \bar{R} + 2\bar{R}\sin^2\left(\frac{\overline{(\psi_k - \alpha t_k)} - \beta}{2}\right),$$

where $\bar{R}$ and $\overline{(\psi_k - \alpha t_k)}$ are the modulus and phase of the complex sum

$$\frac{1}{K}\sum_{k=1}^{K} e^{j(\psi_k - \alpha t_k)} = \bar{R}e^{j\overline{(\psi_k - \alpha t_k)}}. \tag{A5}$$

[79] From equation (A4), it can be seen that for a given slope α, the minimum variance occurs when $\beta = \overline{(\psi_k - \alpha t_k)}$ and that this variance is $1 - \bar{R}$, with $\bar{R}$ given by equation (A5). The best fit is thus obtained by iterating α to determine the value that gives the maximum value of $\bar{R}$ in equation (A5), with β then being given by the corresponding directional mean $\overline{(\psi_k - \alpha t_k)}$ such that the variance is then minimized, given by $V_{min} = 1 - \bar{R}_{max}$.

Appendix B: Phase Models

[80] In Table B1, we provide the parameters of the piecewise linear phase models for the northern and southern oscillations obtained in this paper from fits to the phase data shown in Figure 6. The northern and southern phases are expressed as

$$\Phi_{n,s}(t) = \Phi_{0n,s} + g_{n,s}t = \Phi_{0n,s} + \left(\frac{360 \times 24}{\tau_{n,s}(\text{hr})}\right)t, \tag{B1}$$

where time t is expressed in days with $t = 0$ corresponding to 00 UT on 1 January 2004, the phase constants $\Phi_{0n,s}$ are expressed in degrees, the phase gradients $g_{n,s}$ in degrees per day, and the corresponding oscillation periods $\tau_{n,s}$ in hours as indicated. Values of $\Phi_{0n,s}$ and $\tau_{n,s}$ are given in the table for the 10 overlapping 150 day data fits during interval E1 shown in Figure 6, indicated as intervals E1–1 to E1–10, together with fits to the data for intervals E2–E4. Values for the north/south amplitude ratio k are also given for each interval in the table.

References

Andrews, D. J., E. J. Bunce, S. W. H. Cowley, M. K. Dougherty, G. Provan, and D. J. Southwood (2008), Planetary period oscillations in Saturn's magnetosphere: Phase relation of equatorial magnetic field oscillations and SKR modulation, *J. Geophys. Res.*, *113*, A09205, doi:10.1029/2007JA012937.

Andrews, D. J., S. W. H. Cowley, M. K. Dougherty, and G. Provan (2010a), Magnetic field oscillations near the planetary period in Saturn's equatorial magnetosphere: Variation of amplitude and phase with radial distance and local time, *J. Geophys. Res.*, *115*, doi:10.1029/2007JA014729.

Andrews, D. J., A. J. Coates, S. W. H. Cowley, M. K. Dougherty, L. Lamy, G. Provan, and P. Zarka (2010b), Magnetospheric period oscillations at Saturn: Comparison of equatorial and high-latitude magnetic field periods with north and south SKR periods, *J. Geophys. Res.*, *115*, A12252, doi:10.1029/2010JA015666.

Andrews, D. J., B. Cecconi, S. W. H. Cowley, M. K. Dougherty, L. Lamy, G. Provan, and P. Zarka (2011), Planetary period oscillations in Saturn's magnetosphere: Evidence in magnetic field phase data for rotational modulation of Saturn kilometric radiation emissions, *J. Geophys. Res.*, *116*, A09206, doi:10.1029/2011JA016636.

Andrews, D. J., S. W. H. Cowley, M. K. Dougherty, L. Lamy, G. Provan, and D. J. Southwood (2012), Planetary period oscillations in Saturn's magnetosphere: Evolution of magnetic oscillation properties from southern summer to post-equinox, *J. Geophys. Res.*, *117*, A04224, doi:10.1029/2011JA017444.

Brandt, P. C., K. K. Khurana, D. G. Mitchell, N. Sergis, K. Dialynas, J. F. Carbary, E. C. Roelof, C. P. Paranicas, S. M. Krimigis, and B. H. Mauk (2010), Saturn's periodic magnetic field perturbations caused by a

rotating partial ring current, *Geophys. Res. Lett.*, *37*, L22103, doi:10.1029/ 2010GL045285.

Burch, J. L., A. D. DeJong, J. Goldstein, and D. T. Young (2009), Periodicity in Saturn's magnetosphere: Plasma cam, *Geophys. Res. Lett.*, *36*, L14203, doi:10.1029/2009GL039043.

Burton, M. E., M. K. Dougherty, and C. T. Russell (2010), Saturn's internal planetary magnetic field, *Geophys. Res. Lett.*, *37*, L24105, doi:10.1029/ 2010GL045148.

Carbary, J. F., and S. M. Krimigis (1982), Charged particle periodicity in the Saturnian magnetosphere, *Geophys. Res. Lett.*, *9*, 1073–1076.

Carbary, J. F., D. G. Mitchell, S. M. Krimigis, and N. Krupp (2007), Electron periodicities in Saturn's outer magnetosphere, *J. Geophys. Res.*, *112*, A03206, doi:10.1029/2006JA012077.

Carbary, J. F., D. G. Mitchell, P. Brandt, C. Paranicas, and S. M. Krimigis (2008a), ENA periodicities at Saturn, *Geophys. Res. Lett.*, *35*, L07102, doi:10.1029/2008GL033230.

Carbary, J. F., D. G. Mitchell, P. Brandt, E. C. Roelof, and S. M. Krimigis (2008b), Periodic tilting of Saturn's plasma sheet, *Geophys. Res. Lett.*, *35*, L24101, doi:10.1029/2008GL036339.

Clarke, K. E., et al. (2006), Cassini observations of planetary-period oscillations of Saturn's magnetopause, *Geophys. Res. Lett.*, *33*, L23104, doi:10.1029/2006GL027821.

Clarke, K. E., D. J. Andrews, A. J. Coates, and S. W. H. Cowley (2010a), Magnetopause oscillations near the planetary period at Saturn: Occurrence, phase and amplitude, *J. Geophys. Res.*, *115*, A08209, doi:10.1029/2009JA014745.

Clarke, K. E., D. J. Andrews, A. J. Coates, S. W. H. Cowley, and A. Masters (2010b), Magnetospheric period oscillations of Saturn's bow shock, *J. Geophys. Res.*, *115*, A05202, doi:10.1029/2009JA015164.

Cowley, S. W. H., D. M. Wright, E. J. Bunce, A. C. Carter, M. K. Dougherty, G. Giampieri, J. D. Nichols, and T. R. Robinson (2006), Cassini observations of planetary- period magnetic field oscillations in Saturn's magnetosphere: Doppler shifts and phase motion, *Geophys. Res. Lett.*, *33*, L07104, doi:10.1029/2005GL025522.

Dougherty, M. K., et al. (2005), Cassini magnetometer observations during Saturn orbit insertion, *Science*, *307*, 1266–1270, doi:10.1126/science.1106098.

Espinosa, S. A., and M. K. Dougherty (2000), Periodic perturbations in Saturn's magnetic field, *Geophys. Res. Lett.*, *27*, 2785–2788.

Fischer, G., D. A. Gurnett, S.-Y. Ye, J. B. Groene, J. D. Menietti, and W. S. Kurth (2012), A possible influence of the Great White Spot on the rotation of Saturn's magnetosphere, *EPSC Abstracts*, *7*, EPSC2012-33, 2012.

Galopeau, P. H. M., and A. Lecacheux (2000), Variations of Saturn's radio rotation period measured at kilometer wavelengths, *J. Geophys. Res.*, *105*, 13089–13101.

Goldreich, P., and A. J. Farmer (2007), Spontaneous axisymmetry breaking of the external magnetic field at Saturn, *J. Geophys. Res.*, *112*, A05225, doi:10.1029/2006JA012163.

Gurnett, D. A., W. S. Kurth, and F. L. Scarf (1981), Plasma waves near Saturn: Initial results from Voyager 1, *Science*, *212*, 235–239.

Gurnett, D. A., A. M. Persoon, W. S. Kurth, J. B. Groene, T. F. Averkamp, M. K. Dougherty, and D. J. Southwood (2007), The variable rotation period of the inner region of Saturn's plasma disk, *Science*, *316*, 442–445, doi:10.1126/science.1138562.

Gurnett, D. A., A. Lecacheux, W. S. Kurth, A. M. Persoon, J. B. Groene, L. Lamy, P. Zarka, and J. F. Carbary (2009a), Discovery of a north–south asymmetry in Saturn's radio rotation period, *Geophys. Res. Lett.*, *36*, L16102, doi:10.1029/2009GL039621.

Gurnett, D. A., A. M. Persoon, J. B. Groene, A. J. Kopf, G. B. Hospodarsky, and W. S. Kurth (2009b), A north–south difference in the rotation rate of auroral hiss at Saturn: Comparison to Saturn's kilometric radio emission, *Geophys. Res. Lett.*, *36*, L21108, doi:10.1029/2009GL040774.

Gurnett, D. A., et al. (2010a), A plasmapause-like density boundary at high latitudes in Saturn's magnetosphere, *Geophys. Res. Lett.*, *37*, L16806, doi:10.1029/2010GL044466.

Gurnett, D. A., J. B. Groene, A. M. Persoon, J. D. Menietti, S.-Y. Ye, W. S. Kurth, R. J. MacDowell, and A. Lecacheux (2010b), The reversal of the rotational modulation rates of the north and south components of Saturn kilometric radiation near equinox, *Geophys. Res. Lett.*, *37*, L24101, doi:10.1029/2010GL045796.

Gurnett, D. A., J. B. Groene, T. F. Averkamp, W. S. Kurth, S.-Y. Ye, and G. Fischer (2011), The SLS4 longitude system based on a tracking filter analysis of the rotational modulation of Saturn kilometric radiation, in *Planetary Radio Emissions VII*, edited by H. O. Rucker, W. S. Kurth, P. Louarn, and G. Fischer, pp. 51–64, Austrian Acad. Sci. Press, Vienna.

Jia, X., M. G. Kivelson, and T. I. Gombosi (2012), Driving Saturn's magnetospheric periodicities from the upper atmosphere/ionosphere, *J. Geophys. Res.*, *117*, A04215, doi:10.1029/2011JA017367.

Kanani, S. J., et al. (2010), A new form of Saturn's magnetopause using a dynamic pressure balance model, based on in situ, multi-instrument Cassini measurements, *J. Geophys. Res.*, *115*, A06207, doi:10.1029/ 2009JA014262.

Khurana, K. K., D. G. Mitchell, C. S. Arridge, M. K. Dougherty, C. T. Russell, C. Paranicas, N. Krupp, and A. J. Coates (2009), Sources of rotational signals in Saturn's magnetosphere, *J. Geophys. Res.*, *114*, A02211, doi:10.1029/2008JA013312.

Krupp, N., et al. (2005), The Saturnian plasma sheet as revealed by energetic particle measurements, *Geophys. Res. Lett.*, *32*, L20S03, doi:10.1029/ 2005GL022829.

Kurth, W. S., A. Lecacheux, T. F. Averkamp, J. B. Groene, and D. A. Gurnett (2007), A Saturnian longitude system based on a variable kilometric radiation period, *Geophys. Res. Lett.*, *34*, L02201, doi:10.1029/2006GL028336.

Kurth, W. S., T. F. Averkamp, D. A. Gurnett, J. B. Groene, and A. Lecacheux (2008), An update to a Saturnian longitude system based on kilometric radio emissions, *J. Geophys. Res.*, *113*, A05222, doi:10.1029/2007JA012861.

Lamy, L. (2011), Variability of southern and northern SKR periodicities, in *Planetary Radio Emissions VII*, edited by H. O. Rucker, W. S. Kurth, P. Louarn, and G. Fischer, pp. 39–50, Austrian Acad. Sci. Press, Vienna.

Mardia, K. V., and P. E. Jupp (2000), *Directional Statistics*, J. Wiley and Sons Ltd, Chichester, UK.

Masters, A., N. Achilleos, M. K. Dougherty, J. A. Slavin, G. B. Hospodarsky, C. S. Arridge, and A. J. Coates (2008), An empirical model of Saturn's bow shock: Cassini observations of shock location and shape, *J. Geophys. Res.*, *113*, A10210, doi:10.1029/2008JA013276.

Nichols, J. D., J. T. Clarke, S. W. H. Cowley, J. Duval, A. J. Farmer, J.-C. Gérard, D. Grodent, and S. Wannawichian (2008), Oscillation of Saturn's southern auroral oval, *J. Geophys. Res.*, *113*, A11205, doi:10.1029/2008JA013444.

Nichols, J. D., B. Cecconi, J. T. Clarke, S. W. H. Cowley, J.-C. Gérard, A. Grocott, D. Grodent, L. Lamy, and P. Zarka (2010a), Variation of Saturn's UV aurora with SKR phase, *Geophys. Res. Lett.*, *37*, L15102, doi:10.1029/2010GL044057.

Nichols, J. D., S. W. H. Cowley, and L. Lamy (2010b), Dawn-dusk oscillation of Saturn's conjugate auroral ovals, *Geophys. Res. Lett.*, *37*, L24102, doi:10.1029/2010GL045818.

Provan, G., D. J. Andrews, C. S. Arridge, S. W. H. Cowley, S. E. Milan, M. K. Dougherty, and D. M. Wright (2009a), Polarization and phase of planetary period oscillations on high latitude field lines in Saturn's magnetosphere, *J. Geophys. Res.*, *114*, A02225, doi:10.1029/2008JA013782.

Provan, G., S. W. H. Cowley, and J. D. Nichols (2009b), Phase relation of oscillations near the planetary period of Saturn's auroral oval and the equatorial magnetospheric magnetic field, *J. Geophys. Res.*, *114*, A04205, doi:10.1029/2008JA013988.

Provan, G., D. J. Andrews, B. Cecconi, S. W. H. Cowley, M. K. Dougherty, L. Lamy, and P. Zarka (2011), Magnetospheric period magnetic field oscillations at Saturn: Equatorial phase 'jitter' produced by superposition of southern- and northern-period oscillations, *J. Geophys. Res.*, *116*, A04225, doi:10.1029/2010JA016213.

Provan, G., D. J. Andrews, C. S. Arridge, A. J. Coates, S. W. H. Cowley, G. Cox, M. K. Dougherty, and C. M. Jackman (2012), Dual periodicities in planetary-period magnetic field oscillations in Saturn's tail, *J. Geophys. Res.*, *117*, A01209, doi:10.1029/2011JA017104.

Sandel, B. R., and A. L. Broadfoot (1981), Morphology of Saturn's aurora, *Nature*, *292*, 679–682.

Sandel, B. R., et al. (1982), Extreme ultraviolet observations from the Voyager 2 encounter with Saturn, *Science*, *215*, 548–553.

Smith, C. G. A. (2010), A Saturnian cam current system driven by asymmetric thermospheric heating, *Mon. Not. R. Astron. Soc.*, *410*, 2315–2329, doi:10.1111/j.1365-2966.2010.17602.x.

Southwood, D. J., and M. G. Kivelson (2007), Saturn magnetospheric dynamics: Elucidation of a camshaft model, *J. Geophys. Res.*, *112*, A12222, doi:10.1029/2007JA012254.

Southwood, D. J. (2011), Direct evidence of differences in magnetic rotation rate between Saturn's northern and southern polar regions, *J. Geophys. Res.*, *116*, A01201, doi:10.1029/2010JA016070.

Wang, Z., D. A. Gurnett, G. Fischer, S.-Y. Ye, W. S. Kurth, D. G. Mitchell, J. S. Leisner, and C. T. Russell (2010), Cassini observations of narrow-band radio emissions in Saturn's magnetosphere, *J. Geophys. Res.*, *115*, A06213, doi:10.1029/2009JA014847.

Warwick, J. W., et al. (1981), Planetary radio astronomy observations from Voyager-1 near Saturn, *Science*, *212*, 239–243.

Warwick, J. W., D. S. Evans, J. H. Romig, J. K. Alexander, M. D. Desch, M. L. Kaiser, M. Aubier, Y. Leblanc, A. Lecacheux, and B. M. Pedersen (1982), Planetary radio astronomy observations from Voyager-2 near Saturn, *Science*, *215*, 582–587.

Ye, S.-Y., D. A. Gurnett, J. B. Groene, Z. Wang, and W. S. Kurth (2010), Dual periodicities in the rotational modulation of Saturn narrowband emissions, *J. Geophys. Res.*, *115*, A12258, doi:10.1029/2010JA015780.

Zarka, P., L. Lamy, B. Cecconi, R. Prangé, and H. O. Rucker (2007), Modulation of Saturn's radio clock by solar wind speed, *Nature*, *450*, 265–267, doi:10.1038/nature06237.